RADIATION METROLOGY OF SMALL ANIMAL MOLECULAR IMAGING AND MOLECULAR RADIOTHERAPY USING MICRO-PET/CT

A Dissertation

by

JORDAN JOSEPH DOUGLAS

Submitted to the Office of Graduate and Professional Studies of
Texas A&M University
in partial fulfillment of the requirements for the degree of

DOCTOR OF PHILOSOPHY

Chair of Committee,	Gamal Akabani
Committee Members,	John Ford
	Craig Marianno
	Michael Deveau
Head of Department,	Yassin Hassan

May 2018

Major Subject: Nuclear Engineering

ABSTRACT

Genetically engineered animal models of diseases are increasingly recapitulating human diseases. With this, *in vivo* preclinical imaging of small laboratory animals has emerged as a critical component of biomedical research because of its noninvasive nature allowing serial assay of animal models and monitoring its safety and effectiveness over the history of the disease. The concept of quantitative molecular imaging is to go beyond displaying images in digital form and to consider the image and extract quantitative information that allows for a better understanding of disease progression and treatment. The aim of this work is to demonstrate the need for the metrology of molecular imaging of animal models using micro-PET/CT devices.

System characteristics are determined within each subsystem, micro-PET and micro-CT, independent of each other, and as integrated systems. The characterization of tissues, composition and density, by micro-CT was determined along with the noise level of the unit. Moreover, the nominal superficial and deep absorbed doses were estimated to assess the confounding effect of multiple scans in animal studies. The Q value, used to convert counts per milliliter to activity per milliliter, was estimated to assess the observed activity present in the animal. The resolution of the micro-PET subsystem was also estimated using a modified Derenzo phantom to assess the uncertainty of the activity distribution within tissues. Once both modalities were characterized separately the coordinate system of each individual system was checked

for spatial accuracy using a cross capillary method. The offset values were then used to establish the same coordinate system for co-registration.

Once both micro-PET and micro-CT image data sets had been verified, they were used to generate a voxel image of the subject for use in the Monte Carlo program, MCNP6, where an absorbed dose map was generated for the radiolabeled compound. Two basic examples are given to demonstrate the use of the voxelized absorbed dose maps for calculating the absorbed dose to any segmented organ of interest, across longitudinal studies. In this way, it was shown that an animal-specific model can be used to accurately calculate the absorbed dose for each time point during a study.

DEDICATION

To my family, for providing the fuel for this journey and many more to come.

ACKNOWLEDGEMENTS

First, I would like to thank my committee chair, Dr. Akabani, and my committee members, Dr. Ford, Dr. Marianno, and Dr. Deveau, for their guidance and support throughout the course of this research, I would not be here without it.

Thanks to the Department of Nuclear Engineering and the Texas A&M Institute for Preclinical Studies for allowing me to conduct my research at their facilities.

Thanks also go to my friends, both here in College Station and elsewhere for making my time at Texas A&M University a great experience and keeping me grounded, humble, and focused on the goal.

Finally, thanks to my family for their constant, and at times undeserved, encouragement and support.

CONTRIBUTORS AND FUNDING SOURCES

This work was supported by a dissertation committee consisting of Professor Gamal Akabani [advisor] and Professors John Ford and Craig Marianno of the Department of Nuclear Engineering and Clinical Associate Professor Michael Deveau of the Department of Small Animal Clinical Sciences.

The micro-CT images of the electron density plugs were provided by Professor Akabani's Spring 2017 NUEN 689 class, Introduction to Molecular Imaging. The CT images of the full electron density phantom were provided by Clinical Associate Professor Deveau.

All other work conducted for the dissertation was completed by the student independently.

Graduate study was supported by a teaching fellowship from the College of Engineering at Texas A&M University.

TABLE OF CONTENTS

Page

Page

LIST OF FIGURES

Page

Page

Page

Page

LIST OF TABLES

Page

Page

1 INTRODUCTION

Molecular imaging can be defined as the *in vivo* visualization, characterization and spatiotemporal quantitative measurement and distribution of biological processes at the molecular and cellular levels, associated with a biochemical, biological, diagnostic, or therapeutic application. During the last three decades, the field of molecular imaging has grown exponentially, and it is now academically listed as an integral part of the biomedical sciences along with genomics, proteomics, and metabolomics.

As part of molecular imaging, radiological imaging has long been an indispensable tool in clinical medicine. In clinical practice, a significant effort has been placed in establishing protocols and standards in 2D and 3D image metrology in radiology, radiotherapy and nuclear medicine; however, at the preclinical level, little effort has been placed to establish such standards and protocols.

In vivo imaging of small laboratory animals has emerged as a critical component of preclinical biomedical research. Small-animal imaging provides a noninvasive means of assaying biological structure and function *in vivo*, yielding qualitative and quantitative, spatiotemporal information on normal and diseased tissues, such as tumors. Because of its noninvasive nature, imaging allows serial (i.e. longitudinal) assay of animal models, such as rodents, over the entire natural history of the disease process, from inception to progression, and monitoring of the effectiveness of treatment strategies or other interventions (with each animal serving as its own control and thereby reducing biological variability). This also serves to minimize the number of experimental animals

required for a study. With the ongoing development of genetically engineered (i.e., transgenic and knockout) rodent models of cancer and other critical diseases, such models are increasingly more realistic in recapitulating the sequelae of the corresponding human disease and the ability to track these disease models long-term is therefore invaluable. Importantly, in contrast to cell or tissue culture-based experiments, studies in intact animals incorporate interacting physiological factors –neuronal, hormonal, nutritional, immunological, etc. – present in the complex *in vivo* milieu. Therefore, the concept of quantitative molecular imaging is to go beyond displaying images in digital form and to consider the image and extract quantitative information that will allow for a better understanding of a disease.

Preclinical molecular imaging requires that imaging data are quantitatively representative of the physical and physiological properties and processes being observed in animal models. This will allow the creation of metadata for quantitative imaging informatics and image markup. In the case of micro-PET/CT, there are two specific imaging modalities that require quantitation and integration. These are micro-CT and micro-PET; where each modality requires specific standardization protocols that will ensure the quantitative quality of the data for integration with each other and other non-imaging modalities.

This dissertation aims to demonstrate the need for standardization and quantification of micro-PET/CT devices at the preclinical level. Optimal methods are proposed for both PET and CT units along with their integration of the data sets. Once standardization is established, acquired images are used to generate a voxel image of the

subject in a Monte Carlo program where a dose map is generated for any specific source, or radiolabeled compound. In this way, a patient specific model is used to more accurately generate the dose to each individual subject and the dose to any region can be easily extracted using segmentation.

1.1 The Relevance of Radiation Metrology in Molecular Imaging and Radiotherapy

Despite large investments in drug development, the overall success rate of drugs remains very low. This high attrition rate is mostly due to a lack of a validated translational continuum yielding unsound and unstructured preclinical research. According to the Pharmaceutical Research and Manufacturers of America, in 2015 there were more than 830 drugs and vaccines being developed for cancer therapy and other diseases. Based on the current attrition rate, many of these drugs will fail during preclinical studies or Phase I/II clinical trials. Furthermore, many approved drugs are withdrawn after unforeseen adverse drug reactions during post-market surveillance, increasing the overall cost of drug development. It has been asked, “Can we do better?”. The answer is yes; however, there is a need to raise the standards for preclinical research by improving the preclinical research environment. Therefore, animal models of diseases with higher disease fidelity and reproducibility are needed. When adequately conceived, animal models can contribute invaluable information to our knowledge of biology and medicine, including the discovery and development of new drugs. High fidelity animal models of diseases can help establish specific biomarkers associated with biological pathways that can help in the diagnosis of diseases and development of drugs. However,

biomarker qualification and drug development, as per US FDA guidelines, is riddled with regulatory processes that can only be addressed through well-conceived and executed preclinical animal studies. The characterization, validation of animal models, and their use in biomedical studies requires non-invasive imaging infrastructure where they can quantitatively be observed and analyzed.

1.1.1 Clinical Efforts

As mentioned above, protocols and standards are not well established at the pre-clinical level. In the United States, the National Institute of Standards and Technology (NIST), Radiation Physics Division, in collaboration with the Quantitative Imaging Network of the Cancer Imaging Program at the National Cancer Institute, are carrying out research efforts in establishing the necessary methods and algorithms for the quantitation of images, such as radiological (planer x-ray, CT, MRI), molecular imaging (planar, SPECT, PET), or hybrid imaging modalities [1-6]. In Europe, the National Physical Laboratory of the UK, established the Molecular Radiotherapy Dosimetry (MRT Dosimetry) Project, which has been working on establishing standards for molecular imaging and molecular radiotherapy under the sponsorship of the "European Metrology Programme for Innovation and Research" (EMPIR) [7, 8].

Significant efforts have been made in quantitative image and lesion segmentation of tumors [9], establishment of basic requirements for institutions carrying out clinical trials using PET/CT imaging [10], and assessment of early response to oncology therapies using FDG-PET/CT [11]. A full description of the quantitative imaging efforts

from multiple groups within the Quantitative Imaging Network are presented in the following references [1-6].

1.1.2 Preclinical Efforts

To expedite the study of biological phenomena, disease etiology, diagnosis and therapy, new observational modalities using *in vivo* animal models are needed. Small animal models, particularly genetically engineered mice, are increasingly recognized as powerful discovery tools in biomedical research. The number of animal models of human diseases has increased exponentially, with an associated dramatic increase in an understanding of their spatiotemporal pathophysiology. In 1998, the US National Institutes of Health (NIH) established the Small Animal Imaging Resource Program (RFA-CA-98-023) to develop and enhance (a) shared imaging research resources to be used by investigators, (b) research related to small animal imaging technology, and (c) training the next generation of professional and technical personnel interested in the science, techniques and use of small animal and molecular imaging. This has led to an extraordinary increase in biomedical research and publications related to small animal imaging and translational research, including nanotechnology-based applications. Major research universities have responded aggressively to this initiative with an associated increase in publications and funding. Small animal molecular imaging has a significant role in drug discovery and development.

Today, most major research institutions across the world have a small animal imaging core facility, which has led to the establishment of molecular imaging programs as a preclinical research area. Molecular imaging provides whole-body phenotyping in

an intact animal, which is more relevant than time consuming *in vitro*/*ex vivo* animal studies. Molecular imaging decreases the workload and accelerates biomedical research, by providing statistically accurate results through longitudinal studies, which can be performed in the same living subject. This has led to a surge in the development and study of molecular imaging probes and contrast agents using novel compounds and nanotechnology-based strategies. As a consequence, the NIH established the Molecular Imaging and Contrast Database (MICAD) to classify the more than 4,250 probes that have been developed by major imaging modality (i.e., PET, SPECT, MRI, optical, etc.) and targeting mechanisms. Furthermore, these core facilities have helped the development of nanotechnology-based strategies, which further led to the establishment of the NCI Nanotechnology Characterization Laboratory (https://ncl.cancer.gov) that is dedicated to assessing the immunotoxicity and overall safety and efficacy of nanotechnology-formulated drugs and nanoparticles used in cancer diagnosis, theranostics and therapy [12-20].

Molecular imaging provides continuity for the *in vivo* evaluation of animal models of diseases, safety and efficacy drugs. Small animal models of disease can help evaluate the physiological and metabolic effects and cytotoxic response to drugs, including radiotherapy, chemotherapy, and immunotherapy agents to those in humans. This translational stage, in turn, may help reduce the high attrition rates for novel cancer diagnostic and therapeutic drugs.

An effort has been placed in characterizing many preclinical molecular imaging devices, such as micro-PET/CT; however, the characterization does not include the

specific radionuclides in combination with animal models. For example, a conversion factor can be determined to convert machine counts into an activity concentration for NaF in a water phantom but when injected into a subject, this compound will seek out and attach to bone surfaces. With bone on one side of the compound and tissue on the other, the attenuation values and coincidence counts will be different than those measured in the pure water phantom causing a misrepresentation of the total activity present. New standards and methods need to be developed to incorporate the quantitative values of the micro-PET/CT associated with the subject being studied.

1.2 Animal Models of Diseases

Animal models of human diseases are a fundamental pillar in preclinical studies. They have helped characterize the pathophysiology of many diseases, allowing us to understand their etiology, molecular pathways, mechanism of action, and study the safety and efficacy of drugs. However, there has been significant and valid criticism regarding their use; this criticism has been substantiated by using animal models that lack disease fidelity, reproducibility of research findings, and failure in predicting or correlating with human clinical trials. It has been asserted that researchers are culpable of wasting time, money, animal resources, and, therefore, slowing the scientific progress by presenting non-reproducible data, and thus misinforming other researchers and the public at large. A succinct review of the current ethical issues in animal experimentation is given in Akhtar [21]. These criticisms have led to the establishment of collaborative groups, such as CAMARADES (Collaborative Approach to Meta-Analysis and Review

of Animal Data from Experimental Studies), which carries systemic reviews and meta-analysis from experimental animal models. The group advocates for the use of high fidelity animal models and randomization in preclinical trials to ensure reproducibility and reduce bias. Moreover, the group showed in a systemic review of preclinical animal studies that few well-defined and conceived studies are predictive of clinical efficacy in human clinical trials. These criticisms have led many high-impact scientific journals to demand substantial statistical proof of research findings by means of longitudinal preclinical studies, and well-established biological endpoints by means of non-invasive quantitative in vivo molecular imaging.

In general, experimentation with animal models falls under two categories. These are 1) basic experimentation, which is directed at investigations in basic biology and human disease, and 2) applied experimentation, which is directed at investigating drug research and development, and toxicity and safety testing. Regardless of the focus, animal experimentation is intended to inform human biology and health sciences and to promote the safety and efficacy of potential treatments. There is a plethora of animal models of diseases, and each animal model is amenable for some type of molecular imaging [22-40]. There are pertinent animal models of diseases, including immunological, neurological, mental disorders [41], models of cancer and cancer prevention [42, 43]. Animal models are divided into three convenient groups. These are 1) experimentally induced animal models, 2) spontaneous animal models, and 3) genetically engineered animal models using CRISPR/Cas-9 gene editing [44-46].

1.3 Molecular Imaging Probes

A fundamental area of molecular imaging is the development of molecular probes to assess the pathophysiology of disease and disease response to therapies. Molecular imaging probes help scientists better understand cellular processes and how therapeutic drugs modulate those processes or pathways in a relevant biological context. The basic composition of a molecular imaging probe is based on a signaling agent attached to a specific targeting moiety using a linker. Signaling agents can be based on PET, SPECT, optical, MR, or multimodality agents, and targeting moieties can be viruses, small molecules, peptides, large proteins, antibodies, and even nanoparticles. There are other switch-and-click combinations for developing probes. Molecular probes need to be selected based on their relationship with disease pathophysiology. Many probes are being developed by searching small molecular libraries for a hit compound against a specific target with high affinity. High through-put screening (HTS) is a widely-utilized technology for drug discovery. The establishment of these molecular libraries is by itself a whole research paradigm in medicinal chemistry where molecular imaging plays an important role. Once a target has been validated, HTS is used to search for leading compound candidates. Selected compounds can then be modified by constructing homology models that are amenable for imaging or for the generation of potential drugs.

There is a plethora of molecular imaging probes. In oncology, the primary molecular probe continues to be [^{18}F]FDG-PET/CT; however, there are activity-based molecular probes tagged with other PET radionuclides to visualize programmed cell

death (apoptosis via caspases), inflammation, or for *in vivo* monitoring of EGFR, HER2 or VEGF expression. In cardiology, hybrid [^{18}F]FDG-PET/CT is used as a biomarker for the detection of inflammatory cardiomyopathies, and cardiac sarcoidosis. In neurodegenerative diseases, [^{18}F]TSPO-PET/CT has been used to assess brain ischemia and high-grade glioma, and neuro-inflammation due to Alzheimer's and Parkinson's disease.

Another emerging area in molecular imaging is the assessment of microbial based cancer therapies. The use of bacteria in the regression of certain forms of cancer has been recognized for more than a century. There were many anecdotal studies in the past but now it has been shown that commensal bacterial induces homeostasis, which can prevent cancer induction, progression and regression. Bacteria can also be used as vectors by loading them with natural products such as therapeutics, which is an appealing strategy.

1.4 Quantitative Imaging Biomarkers (QIB)

Detecting a disease, including cancer, at an early stage is one of the most important issues for increasing the recovery and survival rate of patients. Cancer biomarker detection helps to provide a diagnosis before the disease becomes incurable in later stages. Molecularly targeted cancer drugs are often developed with companion diagnostics that attempt to identify which patients will have a better outcome on the new drug than the control regimen. Such predictive biomarkers are playing an increasingly important role in precision medicine. For diagnostic tests, sensitivity, specificity,

positive predictive value (PPV), and negative predictive value (NPV) are usually used as performance measures. For the case of imaging predictive biomarkers, they also need to be characterized for their specificity, sensitivity, PPV, and NPV [47]. Examples of imaging biomarkers are those associated with cognitive decline, such as Alzheimer's disease.

In drug discovery and development, biomarkers play a crucial role in understanding the mechanism of action of a drug, identifying efficacy or toxicity signals at an early stage of development and in identifying patients likely to respond to a specific treatment. The biomarker definitions working group of the NIH established the following definition of a biomarker.

> *Biological marker (biomarker): A characteristic that is objectively measured and evaluated as an indicator of normal biological processes, pathogenic processes, or pharmacologic responses to a therapeutic intervention [48].*

The term 'biomarker' covers a very wide range of data types, uses and applications across all stages of pharmaceutical development. Biomarkers are categorized into the following 1) Prognostic biomarker: Predicts the likely disease prognosis independent of the mode of treatment, 2) Predictive biomarker: Predicts the likelihood of response to a treatment or class of treatments, and 3) Pharmacodynamic biomarker: Responds overtime to a treatment intervention.

Biomarkers can further be divided depending on the mode of data collection [49]. Three types of biomarkers can be recognized 1) Biochemical or histological parameters detected on tissue samples obtained from biopsy or surgery samples, 2) Biochemical parameters or cells obtained on blood or urine samples, and 3) Anatomical, functional or molecular parameters detected with imaging.

In a recent article, the Quantitative Imaging Biomarkers Alliance Working Group (QIBA) of the Radiological Society of North America (RSNA) described the relevant metrological concepts and methods needed for evaluating and comparing QIBs, and discussed the issues associated with the technical performance related to imaging biomarkers [50, 51].

Development of imaging biomarkers is an organized process in which new biomarkers are discovered, verified, validated and qualified against biological processes and clinical end-points [52]. The validation process not only concerns the determination of the sensitivity and specificity, but also the measurement of repeatability and reproducibility. Reproducibility assessments and standardization of the acquisition and data analysis methods are crucial when imaging biomarkers are used in multicenter trials for assessing response to treatment. Quality control in multicenter trials can be performed with the use of imaging phantoms or other techniques. The cost-effectiveness of imaging biomarkers also needs to be determined. Many imaging biomarkers are currently being developed, but there are still unmet needs—for example, in the detection of tumor invasiveness and migration, and dissemination, including the detection of micro-metastasis.

A consensus statement was recently published to address the lack of validated imaging biomarkers shown in O'Connor *et al*. [53]. The need to validate potential imaging biomarkers requires quantitative molecular imaging protocols using well established and characterized animal models of cancer.

1.5 Molecular Imaging Using micro-PET/CT

Today, many pre-clinical systems consist of a micro-PET and micro-CT subsystem for full whole-body imaging of rats and mice. Commercial units are provided by Perkin-Elmer, Sofie Biosciences, Mediso, Bruker, TriFoil Imaging, and MILabs Inc. All current modern micro-PET subsystems use silicon photomultipliers with a 3-D (x-y-z) depth-of-interaction algorithm for an optimized line of registration. The nominal and maximum resolution of current modern micro-PET systems is 1 mm and 0.4 mm, respectively. On the other hand, the micro-CT subsystem consists of a variable or multiple fixed energy x-ray unit and a high-resolution flat panel detector. All current micro-CT subsystems generate images using cone-beam reconstruction algorithms (CBCT) [54]. The CT images are used for tissue characterization, PET attenuation correction and image fusion. All micro-PET/CT units have an integrated anesthesia and physiological monitoring system for each animal bed. Some systems with a large bore are capable of simultaneously scanning for up to four mice using an integrated 4-bed unit. All units are capable of quantitative imaging for ^{18}F by transforming counts per unit volume into activity concentration (Bq/ml). The imaging systems have minimal quality control routines for CT, SPECT and PET to assure reliable data acquisition. However,

many systems are now upgrading the quality control routines by establishing a comprehensive quality assurance (QA) metrology package for quality control (QC). Figure 1 shows an overview of the Albira Si micro-PET/SPECT/CT unit that will be used for this research.

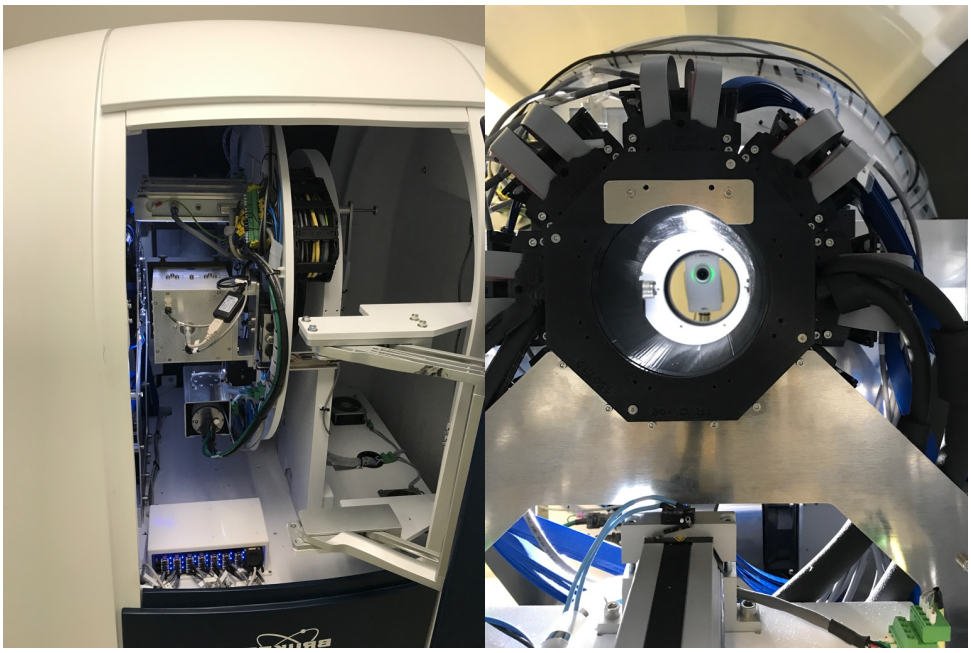

Figure 1. An overview of the Albira Si micro-PET/SPECT/CT unit used in these studies. The system consists of 1) a micro-CT unit consisting of an x-ray and flat panel detector, 2) a 3-ring PET subsystem, and 3) a SPECT subsystem with two cameras.

2 MATERIALS AND METHODS

2.1 Cone Beam Computed Tomography

Computed tomography (CT) is a radiological x-ray imaging technique which consists of an x-ray emitting source and a detector. Current clinical third and fourth generation scanners use a fan beam x-ray in combination with a large array of detectors across the fan width. The x-ray tube and detectors are rigidly linked and undergo single rotation motion. As the emitted x-rays pass through an object, they are attenuated following the standard photon interactions: photoelectric absorption, coherent scattering, and incoherent scattering. The x-rays that make it through the object are measured at the detector and are used to generate projections at different angles of the object. To reject scatter radiation, current systems count with anti-scatter septa, which act as a grid. The reconstruction of the images is based on multiple methods and, in the majority of cases, each machine uses proprietary methods for image reconstruction. Independent of the reconstruction method, all systems need to be calibrated to respond invariantly to the same tissues encountered in the body. This means that no matter the reconstruction method, with the same input every machine should give the same output. Image reconstruction should provide an intrinsic and invariant attenuation coefficient for every voxel of an image. Based on such a premise of invariance, Sir Godfrey Hounsfield established that all reconstruction methods should respond equivalently and thus established the Hounsfield Unit (HU). The HU value has a simple relationship with

water as a reference material. The equation indicates that the values at each location, or voxel, in a CT image are normally given as

$$\mathrm{HU} = \frac{(\mu_{\mathrm{m}} - \mu_{\mathrm{w}})}{(\mu_{\mathrm{w}} - \mu_{\mathrm{a}})} * 1000. \quad (1)$$

Equation 1 shows how to calculate the Hounsfield Unit of a material using the total linear attenuation cross-section for the material, μ_m, water, μ_w, and air, μ_a. Using this equation, water will always have a HU value of 0 while air will always have a HU value of -1000 [56-58]. This allows for a consistent scale relative to the attenuation of water and for comparisons to be made across different machines and reconstruction algorithms. The use of the HU system is largely associated with clinical CT scanners using axial and helical tomographic methods.

The characterization of tissue compositions using CT depends on multiple parameters, including effective x-ray energy and spectrum, detector system, acquisition parameters and reconstruction methods. Any reconstruction method should be invariant and estimate the effective photon attenuation coefficient of the tissues of a specimen, irrespective of location. However, there are significant variations in Hounsfield Units among different CT systems. The micro-CT subsystem of the Albira Si micro-PET/SPECT/CT uses cone-beam CT (CBCT) as the scanning geometry. However, the application of the HU system in CBCT systems is controversial as it does not produce axial tomographic projections. Nonetheless, the HU system is still applicable for metrological purposes.

The x-ray unit of the micro-CT is an Apogee 5500 Series Model 93501 (Oxford Instruments, Oxfordshire, UK) running at 50 W, with energy range between 10 and 50 kVp and two preset energy settings at 35 and 45 kVp. It runs with a maximum current of 1 mA. The target is made of tungsten with an electron incidence angle of 12°. The focal spot is 35 μm. The system has filters of beryllium of 127 μm and aluminum of 500 μm.

The flat panel detector is a Hamamatsu digital flat panel model C7942CK-12 using a single CsI crystal with a matrix of 2400 × 2400 pixels with 12-bit depth capable of 2 frames per second with no binning or 9 frames per second with a 4 × 4 binning. The pixel size is 50 × 50 μm and the resolution at 5% Contrast Transfer Function (CTF) is estimated at 8 line-pairs per mm. The integral noise of the detector per normal acquisition is estimated at 1100 electrons per pixel.

Reconstructed images have a nominal voxel resolution of 90 μm with a minimum of 5 μm. The field of view is 70 x 70 mm [55]. It is the latest emerging technique in computed tomography providing larger axial coverage, shorter scan time, isotropic spatial resolution, and better dose optimization.

2.1.1 Phantoms Utilized in the Present Study

The characterization of any radiological imaging device requires the use of phantoms. In this study two phantoms were available for use. The first was the CIRS Model 62 electron density phantom that consists of 12 tissues in 25 plugs. These tissues were water, lung inhale and exhale, breast, adipose tissue, liver, muscle, trabecular bone, and 4 different dense bone tissues. Figure 2 shows the phantom used in the present

study with internal and external plugs. The plugs were used in our studies as individual elements and they were place individually in the micro-CT.

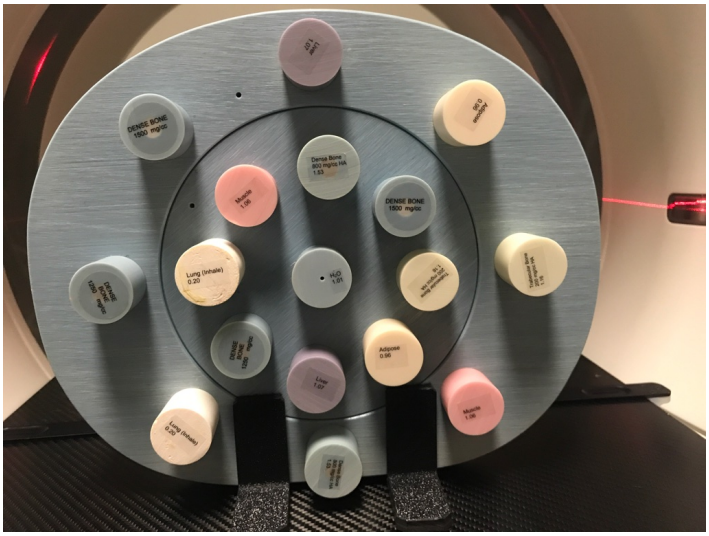

Figure 2. CIRS electron density phantom used to assess the HU using multiple plugs corresponding to different ICRU tissue equivalent materials.

The other phantom used in the present study was a micro-CT HA phantom (Quality Assurance in Radiology and Medicine, QRM, Munich, Germany) shown in Figure 3, which consisted of a single cylinder with 5 internal plugs of different hydroxyapatite (HA) densities of 0, 50, 200, 800 and 1200 mg cm^{-3}. The phantoms were used to compare potential discrepancies in the response of the micro-CT to size and geometry, x-ray potential (tube voltage), and calibration of the unit.

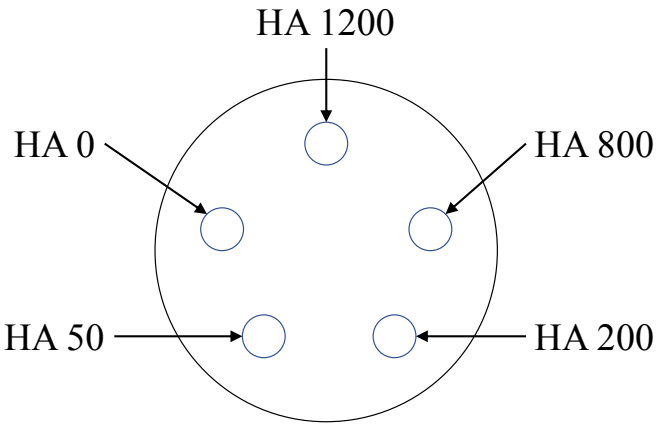

Figure 3. Micro-CT HA phantom used to assess the micro-CT response to different HA densities. The HA densities were 0, 50, 200, 800, and 1200 mg cm^{-3}. Adapted from [59].

2.1.2 HU Linearity

In preclinical scanners, linearity is a significant problem for dense bone structures as CBCT values are not equivalent to those obtained in clinical CT systems. The radio-density measured in CBCT is considered to be inaccurate because different areas of the scan may appear to have different greyscale values depending on their relative positions, even though both locations have the same density and composition [60]. Beam hardening results from the preferential absorption of low energy x-rays as they traverse the object. This effect makes the same tissue to appear with heterogeneities of the HU number and this correction for such artifact is necessary. This is referred as "cupping" artifact. This effect is intrinsic to CBCT systems and is not corrected yet by current reconstruction algorithms, such as COBRA (Exxim Computing Corporation, Pleasanton CA). The issues arise due to angular x-ray spectrum inhomogeneity, yielding different effective x-ray energies at different angles.

The HU values for different densities were estimated using five different bone electron density plugs from the CIRS phantom and the five different bone equivalent electron density locations in the QRM phantom, with each containing a different concentration of HA. These concentrations are 800, 1250, 1500 and 1750 mg cm^{-3} for the CIRS phantom and 0, 50, 200, 800, and 1200 mg cm^{-3} for the QRM phantom. A CBCT image of a dense bone plug and the QRM phantom are shown in Figure 4 below.

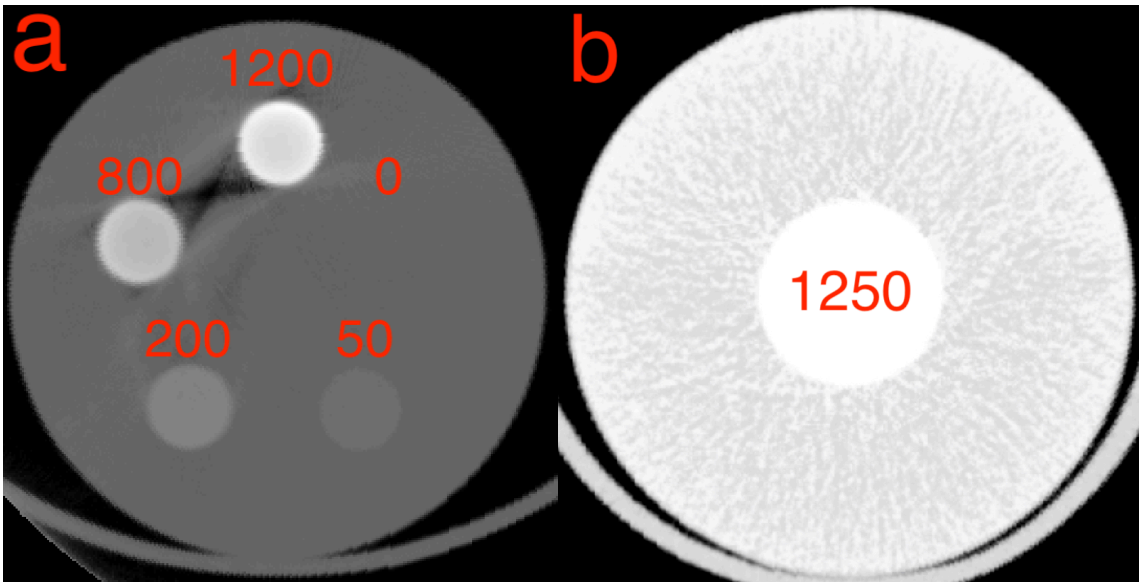

Figure 4. a) CBCT axial image of the QRM micro-CT HA phantom showing the different HA plugs between 0 and 1200 mg cm^{-3}. The diameters of the HA plugs are 5 mm. b) CBCT axial image of the CIRS phantom plug with a HA plug of 1250 mg cm^{-3}. The diameter of the bone plug is 10 mm.

For each phantom, the data was analyzed by drawing a circular ROI occupying more than ~70% of the diameter with the mean count recorded and tabulated along with its standard deviation. The mean counts are plotted against the concentration of HA for

statistical analysis. A linear relationship was expected to show that with a change in material concentration, there is a linear change in the HU value determined by the machine. If linearity is not achieved, it would mean that a change in HU value would not necessarily correspond to the same change in material composition or density.

2.1.3 Image Uniformity and Noise

Image uniformity was visualized using a radial profile drawn over the reconstructed CT slices of a standard water phantom filled with distilled water. A volume rendering of the water phantom is shown below in Figure 5 along with the regions of interest (ROIs) that were used for image analysis.

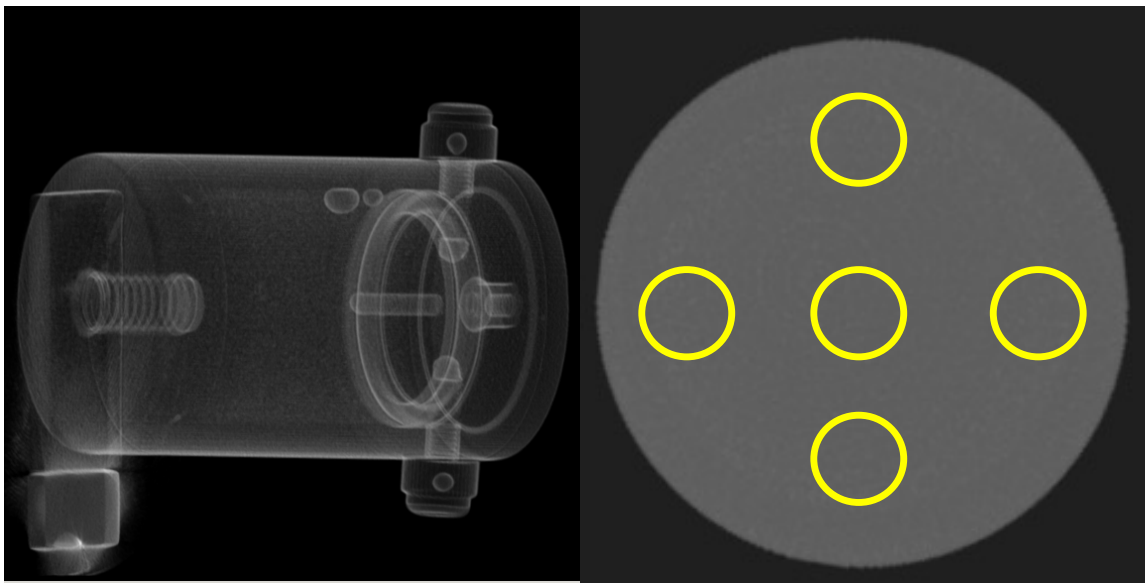

Figure 5. A volume rendering of a water uniformity phantom scan and the location of the five chosen ROI's.

For quantitative assessment, the mean difference in HU value between four peripheral ROIs and a central ROI was computed for the highest current setting, 1 mA, and the highest voltage potential, 45 kVp. The ROI size was approximately 0.92 mm^3 in volume and placed in the north, east, south and west directions. The average difference between the outer ROI's and the inner ROI needs to fall within ± 25 HU of the known value for water, a HU equal to 0. The center value alone must also fall within ± 20 HU of the known value for water.

Image noise is measured from the same five ROI's that were chosen in the uniformity measurement and shown in Figure 5. It is the average of the standard deviation of the five ROI measurements above.

2.1.4 Experimental Tissue Characterization and Uncertainties

The characterization of tissues based on the corrected HU values is fundamental to tissue phenotyping in small animal models of disease. Examples are those associated with animal models of obesity, where fat and lean tissue need to be differentiated, and osteoporosis, for the assessment of bone structures and density. This process of converting from the HU values of each voxel into material composition and densities was based on the measurements from the well-established phantoms. The use of corrected HU values for the characterization of tissues is a complex process that depends, on phantom size and geometry, x-ray voltage and calibration of the unit. Thus, every single micro-CT requires the analysis of the HU value of a given voxel(s) as well as those within a certain region surrounding it.

The physical and electron density of these ICRU tissue equivalent plugs are shown in Table 1 below. A plot of the measured HU value with standard deviation versus the material density was created from this data.

Table 1. CIRS electron density plug values including mass density, electron density and electron density relative to water [61].

	Description	Mass Density ($g\ cm^{-3}$)	Electron Density per cc $\times 10^{23}$	RED (Relative to H_2O)
CIRS Phantom	Lung (Inhale)	0.20	0.634	0.190
	Lung (Exhale)	0.50	1.632	0.489
	Adipose	0.96	3.170	0.949
	Breast (50% Gland / 50% Adipose)	0.99	3.261	0.976
	Water	1.01	3.346	1.002
	Muscle	1.06	3.483	1.043
	Liver	1.07	3.516	1.052
	Trabecular Bone (200 mg/cc HA)	1.16	3.73	1.117
	Dense Bone (800 mg/cc HA)	1.53	4.862	1.456
	Dense Bone (1250 mg/cc HA)	1.83	5.718	1.712
	Dense Bone (1500 mg/cc HA)	2.00	6.209	1.859
	Dense Bone (1750 mg/cc HA)	2.17	6.698	2.005
QRM micro-CT Phantom	Dense Bone (0 mg/cc HA)	1.13	NA	NA
	Dense Bone (50 mg/cc HA)	1.16	NA	NA
	Dense Bone (200 mg/cc HA)	1.26	NA	NA
	Dense Bone (800 mg/cc HA)	1.65	NA	NA
	Dense Bone (1200 mg/cc HA)	1.90	NA	NA

NA: Not available.

2.1.5 Single Pixel Line Profiles

A single pixel line profile was taken in the transverse plane for the QRM micro-CT HA phantom and all available density plugs. A single pixel line profile provides the real HU variability encountered among immediate voxels of a region of interest. Whereas line profiles can be obtained with multiple pixels the resulting average profile will be smooth but not representative of the real variations encountered in the image

data. Figure 6 shows an example of the line profile taken, which includes the air and the density plug. The line profile gives the value of each pixel from left to right. By plotting these values through the different electron density phantoms, the difference in HU value from pixel to pixel across an image can be seen. The effect of beam hardening, the noise level, and tissue differentiation can all be observed from these plots.

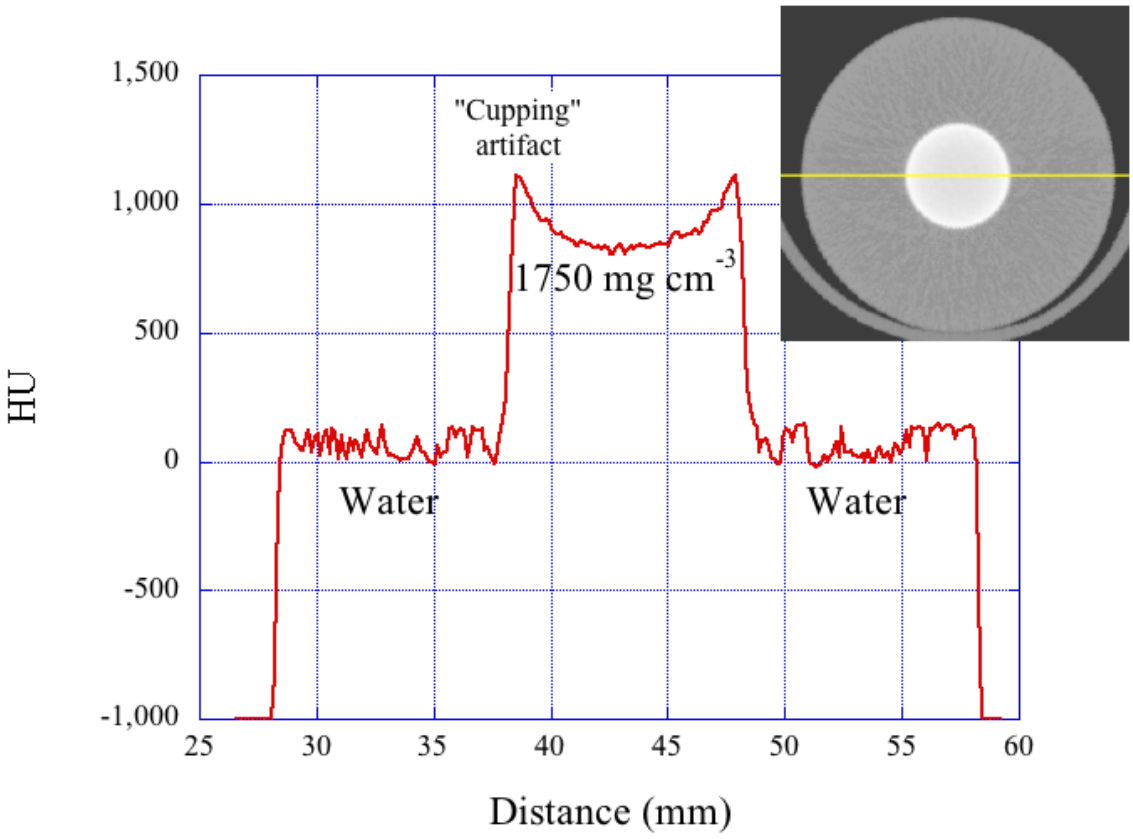

Figure 6. Line profile of a CIRS bone plug with concentration of 1750 mg cm^{-3}. The profile shows the attenuation effects at the edge of the of the internal plug.

2.1.6 Theoretical HU Values as a Function of Material Composition

The HU values for the Albira Si micro-CT were estimated using the ICRU Report 46 [62] composition of the tissues representative in the CIRS Model 062 electron density phantom with material equivalent electron density plugs and the QRM micro-CT HA phantom. The HU values were calculated using the x-ray spectrum generated by the micro-CT using the corresponding electron angle of incidence, filters, and voltage potential. The software used to generate the spectrum was SpekCal [63-65]. Figure 7 shows the x-ray spectrum generated for 35 and 45 kVp using an incent angle of 12 degrees, 127 μm of Be, and 500 μm of Al. The nominal spectra were used to determine the expected HU values of each of the tissue equivalent electron density plugs at the micro-CT levels.

X-ray mass attenuation coefficients were taken from XCOM on the NIST website using the provided tissue composition and energy spectrum values [66]. This produced a list of attenuation coefficients that could be normalized and used to compute the effective linear attenuation coefficient at the effective energy. Those values could then be plugged into Eq. 1 to calculate the HU and give an expected value for each tissue.

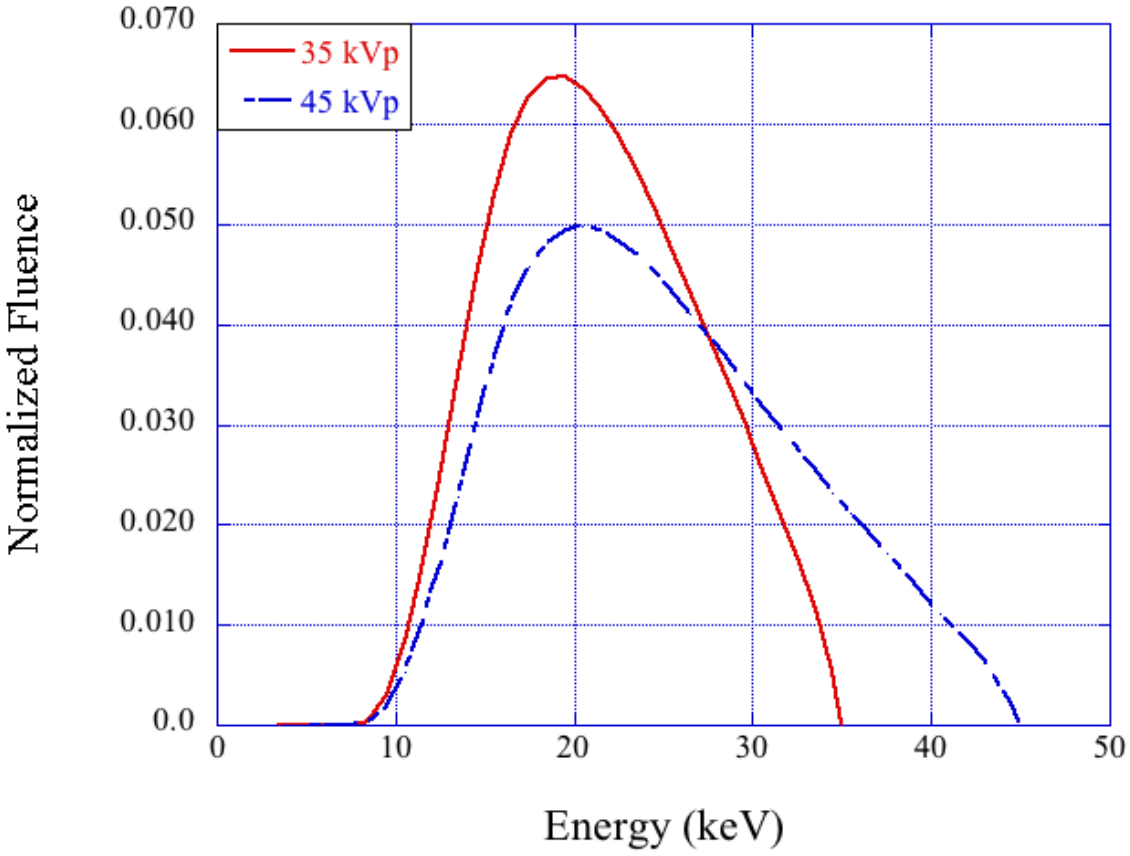

Figure 7. Calculated x-ray spectra for 35 and 45 kVp. The effective energies are 21.4 and 24.8 keV respectively [63-65].

2.1.7 Nominal Absorbed Dose per Scan

Absorbed doses delivered to an animal during longitudinal studies by the micro-CT subsystem are a significant issue as they become a confounding factor during therapeutic or diagnostic studies of radiopharmaceuticals, chemotherapeutics, and immunotherapeutics, which alters the effects of the drug or biomarker. Nominal absorbed doses need to be characterized to address this important confounding factor. A water phantom and an ionization chamber were used to assess the superficial and deep

dose for the CT at low and high current settings with high voltage. This was done as the worst-case scenario, meaning any dose received at other settings should not exceed these values. Calculations for cone-beam CT are simplified because the animal is fixed, and the CT system rotates without any pitch of the bed. Therefore, two specific calculations are of significance in micro-CT, the surface dose and the deep dose.

All measurements were carried out using a calibrated ionization chamber from PTW, model TN31014, with a nominal activate volume of 0.015 cm^3, working at +400 V, with a 100% collection efficiency. The ionization chamber was calibrated using a ^{60}Co unit and the dose conversion factor, $N_{D,W}$, was 2.412×10^9 Gy C^{-1}. The dose meter used was also calibrated at a National Voluntary Laboratory Accreditation Program (NVLAP) with a resulting uncertainty of 0.7% using a ^{137}Cs source. Dosimetry calculations were carried out following the AAPM Protocol for x-ray dosimetry in radiotherapy and radiobiology [67].

The x-ray spectrum that is observed by the flat panel detector changes as it passes through tissue (animal or object), which in turn hardens the primary spectrum. As an example, Figure 8 shows the nominal x-ray spectra for different attenuations through water showing the beam hardening of the original 45 kVp spectrum. The resulting changes are of significance as the average energy of the spectrum increases from 25 to 32 keV. For this reason, both the superficial and deep doses needed to be measured as they each see different x-ray spectra, which deposits the dose at the target location.

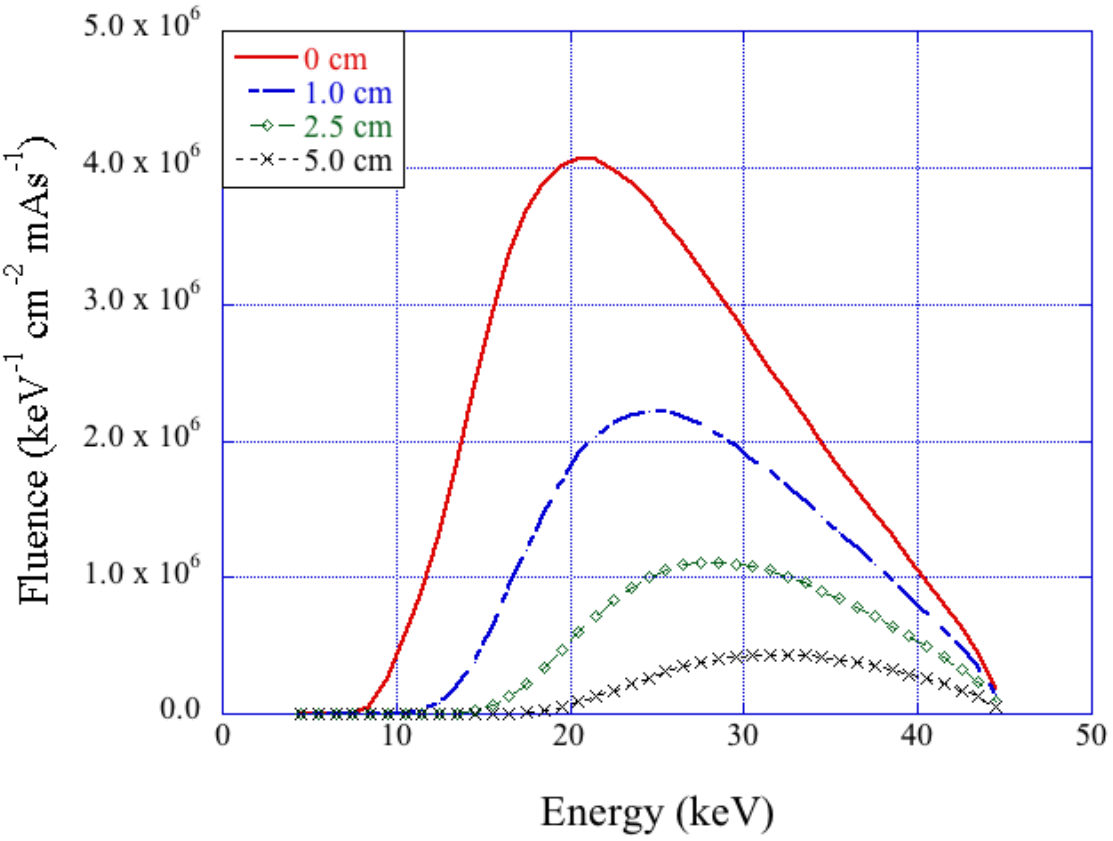

Figure 8. Primary beam hardening of a nominal 45 kVp x-ray spectrum as a function of depth in water. The average energy of the spectrum was estimated at 25, 28, 30, 32 keV for 0, 1, 2.5, and 5 cm depth, respectively.

2.2 Positron Emission Tomography

The micro-PET scanner in the Albira Si unit consist of three individual PET rings, with 8 modules per ring, totaling 24 modules. Each module has its own silicon photomultiplier (SiPM). The combination of continuous crystal, SiPM, and advanced electronics has led to a resolution of 0.7 mm with full field accuracy. The axial field of view is 148 mm and the transaxial view is 80 mm. It can image in three modes, static, dynamic, and dual cardiac/respiratory gated [55]. The National Electrical Manufacturers

Association (NEMA) established the NEMA Standard Publication NU 4-2008 "Performance Measurements of Small Animal Positron Emission Tomographs," which establishes the performance measurements of small animal tomography. The standard calls for the assessment of spatial resolution, sensitivity using a ^{22}Na point source, Scatter Fraction, Count Losses, and Random Coincidence Measurements. However, it does account for radiation metrology of activity of specific radionuclides, such as ^{18}F, ^{124}I, ^{64}Cu, ^{62}Cu, etc.

2.2.1 Calibration and Uncertainties

The detection of photons is highly dependent on total activity, activity concentration, geometry, tissue attenuation and the generation of true, random, and scattered counts. A PET system will correct for these types of counts based on internal algorithms; however, the micro-PET subsystem requires that the system be calibrated to convert counts (counts/ml) into activity (Bq/ml). The micro-PET subsystem was calibrated using a cylindrical phantom with a nominal volume of 99 ml and a total activity concentration of 45473 kBq (1229 μCi). The micro-PET subsystem was allowed to acquire images for 5 min (300 sec) every 30 min for a total elapsed time of 12 hours. Images were reconstructed for a total of 19 data sets. The data is then analyzed using exponential decay and compared with the theoretical values from the decay of the radionuclide, in this study is ^{18}F. The comparison between theoretical values and experimental results provides an estimate of the range of suitable activities and linearity of the system with corresponding errors. The uncertainties are used to assess the

suitability of the images obtained for a given scan and be converted into activity concentrations or SUV values.

2.2.2 Resolution

A Derenzo phantom with different hot rod diameters will be used to measure the resolution, or line pairs per mm, of the micro-PET subsystem. Different activities and reconstruction parameters were run using the same phantom to compare the effects of increasing activity and increasing iterations, or reconstruction time. If these changes have an effect on the calculated activity concentration in a location or the standardized uptake value (SUV) they need to be communicated along with any information obtained from images. Otherwise the values are difficult to reproduce and verify. The basic equation for calculating SUV is

$$SUV = \frac{r}{(a/w)}. \quad (2)$$

In this equation r is the activity concentration in kBq ml^{-1}, a is the decay-corrected activity to time of acquisition in kBq, and w is the weight of the subject in g. In clinical practice SUV values carry great uncertainty and difficult reproducibility as the amount of activity injected depends on many factors. The use of activity concentration tends to be a more reliable variable as it does not depend on the time of administration, uptake time, or uncertainties of activity measurements. For these reasons, activity concentrations will be used in this study.

2.3 micro-CT and micro-PET Image Registration

With each sub-system analyzed individually, the combination of their images and information also needs to be treated with the same precision. That includes how the images are co-registered or combined to overlay the images from the PET and the CT while both images do not actually occur in the same location. Bed movement is required to place the subject at both locations which can be inaccurate and lead to offset images in the three dimensions. Image fusion requires that both sets of data are co-registered in order to assign the activity distribution to the correct tissues and locations. Unfortunately, the resolution of CT images is higher than that of PET images causing mismatches in registration to become more relevant. The fusion of images requires that the virtual isocenter of the micro-PET and micro-CT be the same. The uncertainty in image fusion needs to be estimated when both data sets are registered. The isocenter for both systems will be established using a cross capillary set-up with a minimal activity associated with each. This method, however simple, requires that the capillaries be located within the field of view of each system and be within 2% of the same pixel locations. Co-registration is extremely important for Monte Carlo sampling to assign the correct activity concentration to the corresponding tissue sources. Discrepancies in co-registration can lead to incorrect pharmacokinetic and dosimetry analysis of radiopharmaceuticals or activity on tissues and organs.

2.4 Computational Assessment of Subject Absorbed Dose

Once the CT and PET images have been quantified, they can be used to derive other values of importance to longitudinal studies using the micro-PET/CT, including the dose received for each individual study. To accomplish this objective, we developed a Python script where it reads DICOM images of both CT and PET to create an MCNP input deck for use in MCNP6 (version 6.1) [68]. From MCNP, the absorbed dose to each voxel can be calculated and used to generate plots of distributed absorbed dose to any collection of desired voxels for a given region of interest (ROI).

2.4.1 Reading in a DICOM Image

The first step of the program is to give the location of the PET and CT image stacks and read in all of the required values needed for creating the input deck. For this program, the CT images should be placed in a folder titled “CT” and the PET images should be places in a file titled “PET”. These folders will always remain in the same location as the source code, and each time the program is to be run, the new images should be placed in their correct locations.

Using a package in Python, the images can be read, and any information stored in the DICOM images can be accessed. For this program we need the array values for each slice, the slice location, the pixel spacing, the number of rows and columns, the rescale slope, and the rescale intercept. The slice location allows the program to correctly order each slice no matter what order they are in in the folder. The pixel spacing gives the dimensions of each voxel in millimeters, which needs to be converted to centimeters for

use in MCNP. The number of rows and columns tells us how many voxels are in each slice and the number of files tells us how many slices we haves. The pixel values in a CT DICOM image are converted from HU values before being stored. Therefore, in order to convert these values back to HU, they need to be adjusted by the rescale slope and intercept before they can be used by the program. The pixel array for the PET data needs no conversions and can be used as imported because the data is used as a probability distribution of source location and will retain the same relative value.

2.4.2 Creating an MCNP Run

A description of each major portion of the input deck is provided below with sample code provided for the reader. An in-depth description of how MCNP works is not covered, only a brief overview of the necessary parts to understand and run this code. Figure 9 below will be broken up between the next few sections to describe how this input deck works in the MCNP code.

```
~~~~~~~~~~~~~~~~~~~~~~~~~~~~~~~~ Example Input Deck ~~~~~~~~~~~~~~~~~~~~~~~~~~~~~~~~
C
C ~~~~~~~~~~~~~~~~~~~~~~~~~~~~~~~~ Cell Cards ~~~~~~~~~~~~~~~~~~~~~~~~~~~~~~~~~~~~~~~
C
C A universe containing only air
1 1 -0.001205 -3 u=1
C
C A universe containing only water
2 2 -0.998207 -3 u=2
C
C A lattice made of voxel sized boxes filled with different material universes
3 0           -1 u=3 lat=1 fill=-255:256 -255:256 -106:106 &
1 48379r 2 1r 1 506r 2 7r … … … 1 2r 2 1 463r
C
C Sets the lattice inside the total image box
4 0           -2           fill=3
C
C Sets the world outside the total image to void
5 0            2
```

Figure 9. An Example MCNP input file.

```
C ~~~~~~~~~~~~~~~~~~~~~~~~~~~~~~~~~~~~ Surface Cards ~~~~~~~~~~~~~~~~~~~~~~~~~~~~~~~~~~~~
C
C A box the size of one voxel in the image
1 BOX -0.0293945 -0.0293945 -0.0625 0.058789 0 0 0 0.058789 0 0 0 0.125
C
C A box the size of the total image
2 BOX -15.020615 -15.020615 -13.3125 30.04123 0 0 0 30.04123 0 0 0 26.625
C
C A sphere centered at the origin
3 SO  30.1

C ~~~~~~~~~~~~~~~~~~~~~~~~~~~~~~~~~~~~ Data Cards ~~~~~~~~~~~~~~~~~~~~~~~~~~~~~~~~~~~~
C
C Tracks both photon and electrons
MODE P E
C
C
SDEF ERG=FPAR=D1 CEL=D2 PAR=D3
C Gives the discrete dependent variable of starting energy depending on the
C particle type chosen
DS1 L 5.0E-4 5.24E-4 5.2E-4 2.498E-1
C
C Gives the discrete variable distribution of the starting cell
SI2 L (0<3[-255:256 -255:256 -106:106]<4)
SP2 0 1027r 16 7 12 9 16 6 3 1 0 6r 10 13 4 0 1r 2 5 8 1r 4 0 129r 361 382 &
272 101 85 44 20 12 24 11 12 2 0 7r … … … 3 1 1r 0 120r
C
C Gives the discrete variable distribution of the emitted particle type
SI3 L 2 2 3 8
SP3 4.74E-12 1.8E-4 3.07E-2 9.67E-1
C
C An energy deposition tally in each cell of the lattice in units of MeV
*F8:P,E (3<3[-255:256 -255:256 -106:106])
C
C Air (Dry, Near Sea Level)
M1    6000     0.000150 $C
      7000     0.784431 $N
      8000     0.210748 $O
     18000     0.004671 $Ar
      PLIB 12P ELIB 03E GAS 1
C
C Water, Liquid
M2    1000     0.666657 $H
      8000     0.333343 $O
      PLIB 12p ELIB 03E
C
C The photon and electron importances for each cell
IMP:P,E 1 1 1 1 0
C
C Set's the cutoff energy for photons and electrons to 20 eV
CUT:P,E j 2E-5
C
C Creates a mctal file containing the results of the above tally
PRDMP 2J 1
C
C Runs one million particles before ending the code
NPS 1E6
```

Figure 9. Continued.

Surface Cards

While very long in length, this input deck is actually very simple. It contains only three surfaces, two boxes and a sphere. An example of the surface cards is shown below in Figure 10.

```
C ~~~~~~~~~~~~~~~~~~~~~~~~~~~~~~~~~~~~ Surface Cards ~~~~~~~~~~~~~~~~~~~~~~~~~~~~~~~~~~~~
C
C A box the size of one voxel in the image
1 BOX -0.0293945 -0.0293945 -0.0625 0.058789 0 0 0 0.058789 0 0 0 0.125
C
C A box the size of the total image
2 BOX -15.020615 -15.020615 -13.3125 30.04123 0 0 0 30.04123 0 0 0 26.625
C
C A sphere centered at the origin
3 SO  30.1
```

Figure 10. Example surface cards used in the MCNP input deck.

Surface 1 is a box where the first three entries, (C1, C2, C3), are the (x, y, z) coordinates of the corner of the box, the second three entries, (X, 0, 0), are the vector of the first side, the next three, (0, Y, 0), the vector of the second side, and the last three, (0, 0, Z), the vector of the third side. When (C1, C2, C3) is equal to (-X/2, -Y/2, -Z/2), you create a box centered at the origin with length $X \times Y \times Z$. Surface 1 is set to the size of a single voxel and surface 2 is set to the size of the total image, or the number of voxels in each direction times the size of the voxel in that direction. Surface 3 is a sphere oriented at the origin with a radius of length R, which is used to define the material universes discussed below. No other surfaces are needed in this input deck.

Cell Cards

A sample cell input is shown below in Figure 11. This is not what the final version of the MCNP input deck looks like but serves to accurately demonstrate the important points of the input deck.

```
C ~~~~~~~~~~~~~~~~~~~~~~~~~~~~~~~~~~~~ Cell Cards ~~~~~~~~~~~~~~~~~~~~~~~~~~~~~~~~~~~~
C
C A universe containing only air
1 1 -0.001205 -3 u=1
C
C A universe containing only water
2 2 -0.998207 -3 u=2
C
C A lattice made of voxel sized boxes filled with different material universes
3 0           -1 u=3 lat=1 fill=-255:256 -255:256 -106:106 &
1 48379r 2 1r 1 506r 2 7r … … … 1 2r 2 1 463r
C
C Sets the lattice inside the total image box
4 0           -2           fill=3
C
C Sets the world outside the total image to void
5 0            2
```

Figure 11. Example cell cards used in the MCNP input deck.

Cell 1, starting on the second line denoted with the number 1, is filled with material 1, which will be specified below, and a density of 1.205×10^{-3} g cm^{-3}. The negative sign on the density value indicates that it is a mass density, as opposed to an atomic density which would be indicated with a positive value. All densities in this program are input as mass densities. The "-3" following the density indicates that this material fills the inside of surface three, which is described above as a sphere centered at the origin. This cell is stored as universe one, as indicated by "u=1". For each material and density combination necessary in the input deck, there will be a specific cell and

universe that corresponds to it. In the example code there are two materials, indicated by cells one and two. Following these is a cell, cell three, which is filled with void, indicated by 0, and is contained inside surface one, which is the voxel box. This cell is a lattice made up of hexahedra's, or cubes. It contains cubes located at position (-255, -255, -106) all the way to (256, 256, 106), or 512 x 512 x 213 = 55,836,672 voxels. The "&" at the end of the line indicates that the input continues onto the next line which describes the universe which fills each position on the lattice. A "1" indicates universe one while a "2" indicates universe 2. A number with an "r" attached to in, as in "48370r" means that the previous position, in this case position 1, should be repeated 48,370 more times. This format was used to reduce the memory size of the input files created since every voxel did not necessarily need to be explicitly written. The positions fill from (-255, -255, -106) to (-254, -255, -106) through all 512 x-direction positions before incrementing once in the y-direction. Once all 512 y-direction positions have been filled, it then increments once in the z-direction position. Figure 12 is a visual example of how the lattice positions are filled.

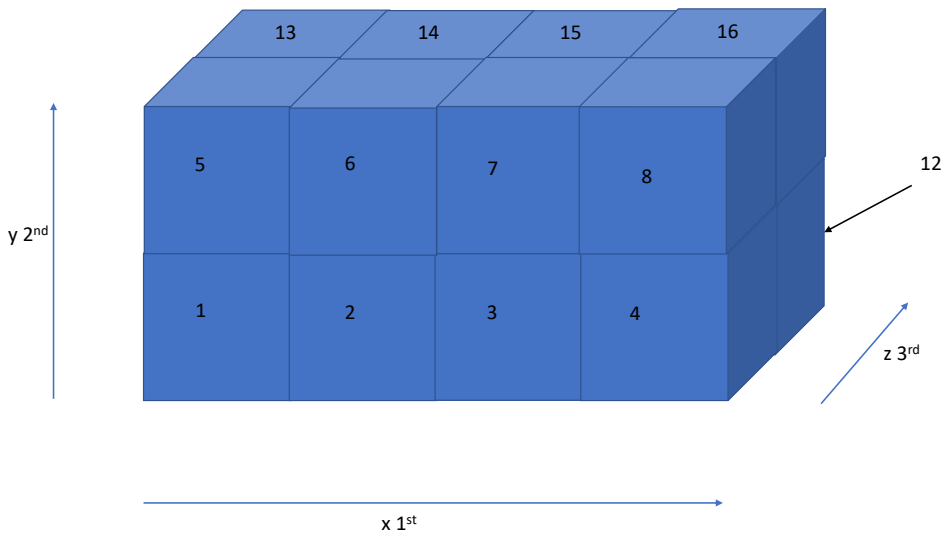

Figure 12. An example of how the lattice fills, starting from position 1 and ending with position 16. It first increments along the x-direction, then increments along the y-direction, and finally in the z-direction.

Cell four puts our lattice structure inside our box which is the size of the total image and cell five makes everything outside of the total image box void. In this way, any particle that leaves the volume defined by the total image box will no longer be tracked by MCNP. The material of each voxel is decided by the value of the pixel array at that location in the DICOM slice. In this way the image is recreated voxel by voxel in MCNP.

Material Specification

Material composition and ranges were determined using the results from Schneider *et al.* [69]. They gave equations for density across the range of HU values as well as a table of different HU values and their compositions. Their table was converted from HU values to density ranges. These density ranges were compared to the plot

generated in from the Tissue Characterization and Uncertainty section. This redistributes their HU ranges into the HU ranges for the Albira Si machine. The material specification lines of the input deck are shown below in Figure 13.

```
C Air (Dry, Near Sea Level)
M1    6000     0.000150 $C
      7000     0.784431 $N
      8000     0.210748 $O
     18000     0.004671 $Ar
      PLIB 12P ELIB 03E GAS 1
C
C Water, Liquid
M2    1000     0.666657 $H
      8000     0.333343 $O
      PLIB 12p ELIB 03E
```

Figure 13. Example material cards used in the MCNP input deck.

The first material, “M1”, represents dry air while material two, “M2”, represents water. The values following the material numbers are in the form of ZAID numbers where the first number is the atomic number of an element, or Z, followed by the mass number, or A. If the natural abundance of an element is desired, then a mass number of “000” should be used.

For example, the ZAID number of natural hydrogen would be 1000. The value following the ZAID number is the atomic fraction, or weight fraction if entered with a negative sign, and indicates the fraction of the material which is composed of the preceding element. The “PLIB” and “ELIB” entries specify the libraries from which the photon and electron data libraries should be acquired. If “GAS” is set equal to one, it indicates that the material should be in a gas state. If it is set to zero or not specified, then the material should be treated as a solid or liquid.

Source Specification

In this code the decay of ^{18}F was modeled as the radioactive source in the problem. It decays by positron emission 96.7% of the time with an energy of 249.8 keV, and by electron capture 3.3% of the time emitting either an Auger electron with energy 0.52 keV, an x-ray with energy 0.5249 keV, or an x-ray with energy 0.5 keV. It has a half-life of 109.77 minutes and its daughter, ^{18}O, is stable. The pixel array of the PET gives the relative distribution of the source throughout the body and can therefore be used as the probability of a particle being emitted from a certain location relative to every other location in the geometry.

An example of the source distribution used in this code is presented in Figure 14 below.

```
SDEF ERG=FPAR=D1 CEL=D2 PAR=D3
C
C Gives the discrete dependent variable of starting energy depending on the
C particle type chosen
DS1 L 5.0E-4 5.24E-4 5.2E-4 2.498E-1
C
C Gives the discrete variable distribution of the starting cell
SI2 L (0<3[-255:256 -255:256 -106:106]<4)
SP2 0 1027r 16 7 12 9 16 6 3 1 0 6r 10 13 4 0 1r 2 5 8 1r 4 0 129r 361 382 &
272 101 85 44 20 12 24 11 12 2 0 7r … … … 3 1 1r 0 120r
C
C Gives the discrete variable distribution of the emitted particle type
SI3 L 2 2 3 8
SP3 4.74E-12 1.8E-4 3.07E-2 9.67E-1
```

Figure 14. Example source cards used in the MCNP input deck.

The “SDEF” line indicates the variables of the source in the geometry including “PAR”, the particle type emitted, “CEL”, the cell in which the particle should start in, and “ERG”, the energy of the particle started. The cell and particle type variables are each given by a distribution, “D2” and “D3” respectively, while the energy distribution, “D1”, is a distribution dependent on the variable particle type, indicated by “FPAR”. The particle type distribution is described by “SI3” and “SP3”. The source information card “SI” gives the discrete variable values while the source probability card “SP” gives the probability for each discrete variable. In this example, the emitted particle can be one of four options, two type two particles, a type three particle, or a type eight particle. Type two is a photon, type three is an electron, and type eight is a positron. The emission probabilities of these particles are 4.74×10^{-10} %, 1.8×10^{-2} %, 3.07 %, and 96.7 % respectively. The energy distribution depends on which particle is emitted, therefore tying the correct emission energy with the different decay paths.

The cell description is given by “SI2” and “SP2”. In this example, every cell is included in the distribution and the PET pixel data is used to give the probability that a source is emitted from that particular voxel. The exact starting location for a source particle is randomly distributed inside whichever cell is chosen for the particle to be born in. This is because while the activity concentration of the PET tracer inside a certain voxel is known, it cannot say from which location inside that voxel the particles were emitted from.

Physics

An example of the physics cards used in the input deck are given below in Figure 15. The "mode" line indicates that the program will track both photons, "p", and electrons "e", but not neutrons. The program treats positrons similar to electrons and will therefore track them as well.

```
C The photon and electron importances for each cell
IMP:P,E 1 1 1 1 0
C
C Set's the cutoff energy for photons and electrons to 20 eV
CUT:P,E j 2E-5
C
C Creates a mctal file containing the results of the above tally
PRDMP 2J 1
C
C Runs one million particles before ending the code
NPS 1E6
```

Figure 15. Example physics cards used in the MCNP deck.

The cut cards indicate the energy below which particles will no longer be tracked. Both photons and electrons will only be tracked down to 20 eV. All other physics interactions are left at their default settings for the program.

Tallies

An *F8 tally is used in this input deck to calculate the energy deposited in each lattice position or voxel and can be seen in Figure 16 below.

```
C An energy deposition tally in each cell of the lattice in units of MeV
*F8:P,E (3<3[-255:256 -255:256 -106:106])
```

Figure 16. Example Tally card used in the MCNP deck.

The asterisk before “f8” indicates that the tally result should be given in units of MeV. The tally tracks the energy deposition by both photons and electrons by the “p,e” following the tally call. The “(3<3[-256:256 -256:256 -106:106])” indicates the locations in the lattice that the tally should occur in. It gives an individual energy deposition tally for each cell listed, which in this case is every cell in the lattice.

Output

The results of the tally in MCNP are printed to the output file with the tally statistics as well as the warnings, comments, and information about the MCNP run. The tally results are also printed to a separate file in ASCII format. This separate ASCII file is used to read in the results for each lattice or voxel position. Each voxel position has a value for the energy deposited per starting particle in MeV and the relative error of the energy deposited. These values are read into arrays, one containing the energy and one containing the error. Each position in the energy array is divided by the mass of that particular voxel in grams, which depends on the material designation from the MCNP input deck. This converts the energy array into a dose array with units of MeV per gram per starting particle. The unit of starting particle can be replaced with the unit of Bq s, or decays. Multiplying by 1.602×10^{-10} converts this into units of Gy Bq^{-1} s^{-1}. This array is saved in the DICOM format and can be loaded into any image viewing software for analysis.

2.4.3 Imaging Studies

Two different studies were analyzed to determine dose and verify that the energy distribution follows as expected based on the tracer type injected. The first study is the tracer Fludeoxyglucose ([^{18}F]FDG) injected retro-obritally while the second is the tracer sodium fluoride ([^{18}F]NaF) injected by tail vein injection. Each PET image and corresponding CT image is used to create an MCNP input deck. That deck is run and the resulting energy deposition per voxel is determined and saved in the DICOM image format. These images can then all be loaded into a program like ITK-SNAP and segmentation can be done to determine the dose to any desired collection of voxels. In this way, if the user would like to change the segmentation a new MCNP run is not necessary to recalculate the dose to the new collection of voxels.

3 RESULTS

Based off of the materials and methods described above the data was gathered and plots were generated. These are provided below with a discussion on the major implications occurring in Section 4.

3.1 Cone Beam Computed Tomography

The CBCT unit was used to quantify the characteristics of the machine for use in pre-clinical studies. The results are discussed in the following subsections. The acquisition quality depends on the number of projections resulting in different exposure time and final reconstructed voxel size. The reconstruction of the data is carried out using the proprietary reconstruction code COBRA (Exxim Computing Corporation, Pleasanton CA). The number of projections is substantial as a cone beam CT is being used and a fraction of the field of view is being used for reconstructing the 3D volume. Table 2 shows the available CT acquisition parameters for the micro-CT subsystem.

Table 2. Nominal CT acquisition specification parameters.

Acquisition Quality	Projections	Approximate Exposure Time (min)	Voxel Size (μm)
Standard	250	3	500
Good	400	5	250
Best	600	8	125
High Resolution (For ex-vivo imaging only)	1000	10	35

3.1.1 Linearity

Using the trabecular bone and four dense bone plugs the HU values for the Albira Si CT machine were tabulated at 35 and 45 kVp for the CIRS phantom and are shown below in Table 3.

Table 3. Linearity values measured from the Albira Si micro-CT at 35 and 45 kVp using CIRS model 62 bone equivalent phantoms plugs with differing HA densities.

Bone Tissues	HA Concentration (mg cm^{-3})	35 kVp		45 kVp	
		Measured Mean HU	HU Standard Deviation	Measured Mean HU	HU Standard Deviation
Trabecular Bone	200	319.61	24.80	318.06	24.69
Dense Bone	800	619.50	65.79	610.54	19.76
	1250	891.82	159.85	739.30	42.89
	1500	996.34	213.61	834.20	42.83
	1750	1090.83	271.76	899.57	53.42

Table 4 shows the HU values for the five plugs in the QRM phantom at 45 kVp. While the concentrations differ between the two phantoms they do share one point in common, 800 mg cm^{-3}, and have another relatively close to each other, ~1200 mg cm^{-3}. From inspection these values do not fall within two standard deviations of each other and can therefore be considered different values.

Table 4. Linearity values measured from the Albira Si micro-CT at 45 kVp using the QRM-HA phantom.

Bone Tissues	HA Concentration (mg cm^{-3})	45kVp Measured Mean HU	45kVp HU Standard Deviation
Dense Bone	50	65.31	7.25
	200	254.55	8.18
	800	828.99	40.19
	1200	1169.3	52.5

These results are also plotted with a linear line of best fit in Figure 17 below. The R^2 values for the lines of best fit area 0.99595, 0.98104, and 0.99752 for the CIRS 35 kVp, CIRS 45 kVp, and the QRM 45 kVp phantom images respectively. While all of the images have a linear trend to them the data for the 1250 mg cm^{-3} value for 45 kVp lies much further from the line than the rest of the points do. This is indicated by an R^2 value closer to 1, for the CIRS 35 kVp and QRM 45 kVp lines. For all cases, with an R^2 above 0.95 it can confidently be said that the data follows a linear trend.

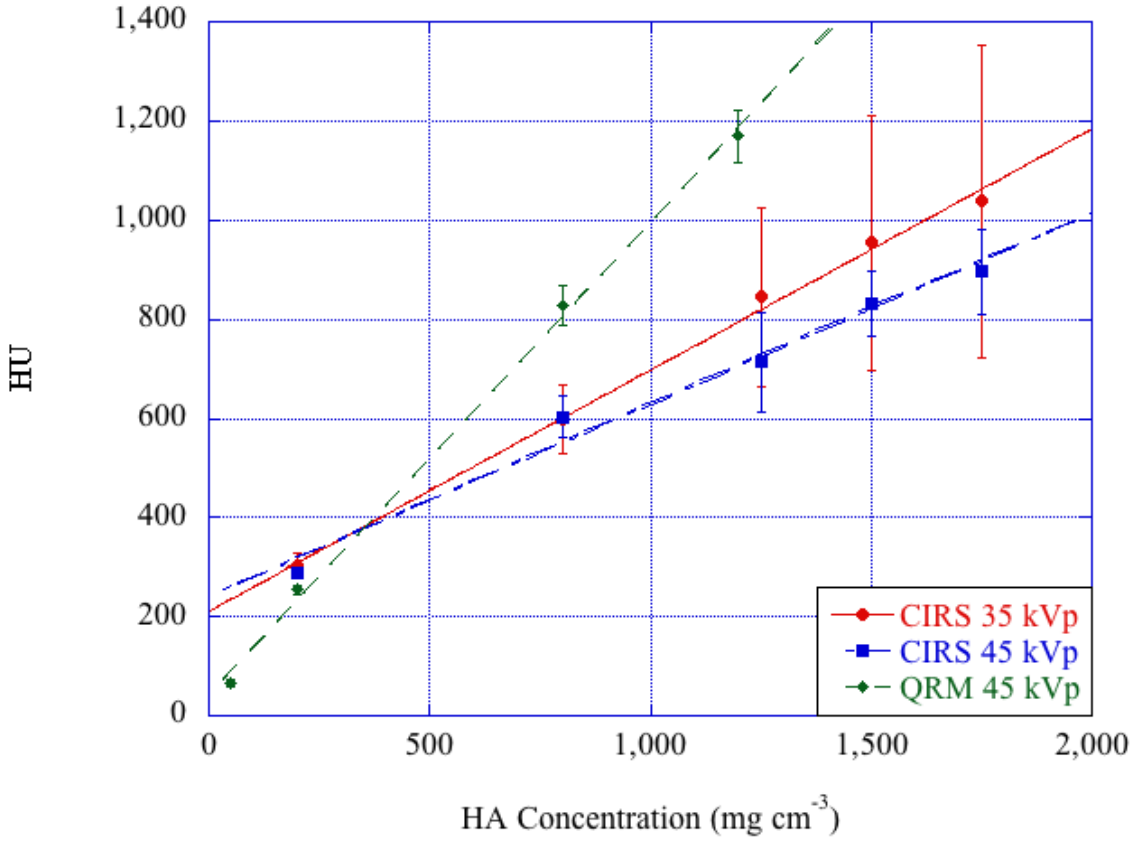

Figure 17. A plot of the HU values of bone equivalent phantoms with different densities of HA inside the CIRS and QRM phantoms with a linear regression fitted to each. The R^2 values for the lines of best fit are 0.99595, 0.98104, and 0.99752 for the CIRS 35 kVp, CIRS 45 kVp, and the QRM 45 kVp phantoms respectively.

This conclusion should allow for values in the HU range of bone to be compared and interpreted without worry that the values are incorrect or misleading. Since the machine calibration occurs between air and water it can also be assumed that those HU value areas also follow an accepted linear trend. All of this is to say that the values produced by this machine should be comparable and represent a real change in density and/or material composition no matter where on the HU range the value should fall.

3.1.2 Image Uniformity and Noise

Using the water phantom with 5 ROI's drawn inside of the water region of the phantom and one region drawn outside in the air, the results in Table 5 were calculated.

Table 5. Uniformity values measured in a water phantom at the center and four directions.

ROI Location	ROI Size (mm^3)	Mean HU	HU Standard Deviation	Difference from Center
Air	0.92456	-1000	0	
Center	0.92395	3.895	19.468	
North	0.92395	26.423	27.527	22.527
East	0.92395	18.503	22.822	14.608
South	0.92395	22.270	25.163	18.374
West	0.92395	25.889	28.758	21.993
Average Difference from Center				19.376

The effects of the CBCT can be seen in the above table. While every location contains only distilled water, the center location has an HU value of 3.895 while every directional location has an HU value in the range of 18 to 27. It can also be seen that the error of the values located towards the outer regions of the image is greater than that of the center value. This shows the effect of the CBCT, where voxel locations towards the outer regions are deemed to have a higher attenuation value than the same material located in the center of the image. When viewing images and conducting segmentation this increase in HU values towards the outer regions of the image could have a major effect on the classification of those voxel positions.

An average distance from the center value of 0 ± 25 HU and a center value of 0 ± 20 HU is acceptable and considered a pass by the system calibrations. By definition this

scan was acceptable and passed the required quality control checks with a value of 19.376, but the user should continue to monitor the calibration. If this value begins to shift significantly further than its current location, values taken from the image will not be deemed reliable.

3.1.3 Experimental HU Values as a Function of Material Composition

The tissue equivalent electron density plugs were measured individually in the micro-CT machine and their mean HU values are shown in Table 6 and Table 7 below. This data is also plotted in Figure 18 with a linear line that intersects the values for both air and water.

Table 6. Electron density phantom measured HU values for each CIRS plug.

Tissue	Mass Density ($g\ cm^{-3}$)	35 kVp Measured HU	35 kVp Standard Deviation	45 kVp Measured HU	45 kVp Standard Deviation
Air	0.00121	-1000	0	-1000	0
Inhale	0.20	-935.51	69.36	-938.79	61.10
Exhale	0.50	-316.95	50.02	-381.39	35.37
Adipose	0.96	-72.91	24.76	-68.38	21.28
Breast	0.99	-23.00	11.50	-25.43	11.28
H_2O Equivalent	1.01	55.53	48.51	39.26	35.80
Muscle	1.06	98.54	43.86	86.37	39.32
Liver	1.07	108.67	39.66	107.11	35.87
Trabecular Bone	1.16	319.61	24.80	318.06	24.69
Dense Bone	1.53	619.50	65.79	610.54	19.76
Dense Bone	1.83	891.83	159.85	739.30	42.89
Dense Bone	2.00	996.34	213.61	834.20	42.83
Dense Bone	2.17	1090.83	271.76	899.57	53.42

Table 7. Electron density phantom measured HU values for each QRM plug.

Tissues	Density (g cm^{-3})	45kVp Measured Mean HU	45kVp HU Standard Deviation
Dense Bone	1.13	-16.66	6.7
Dense Bone	1.16	65.31	7.25
Dense Bone	1.26	254.55	8.18
Dense Bone	1.65	828.99	40.19
Dense Bone	1.90	1169.32	52.5

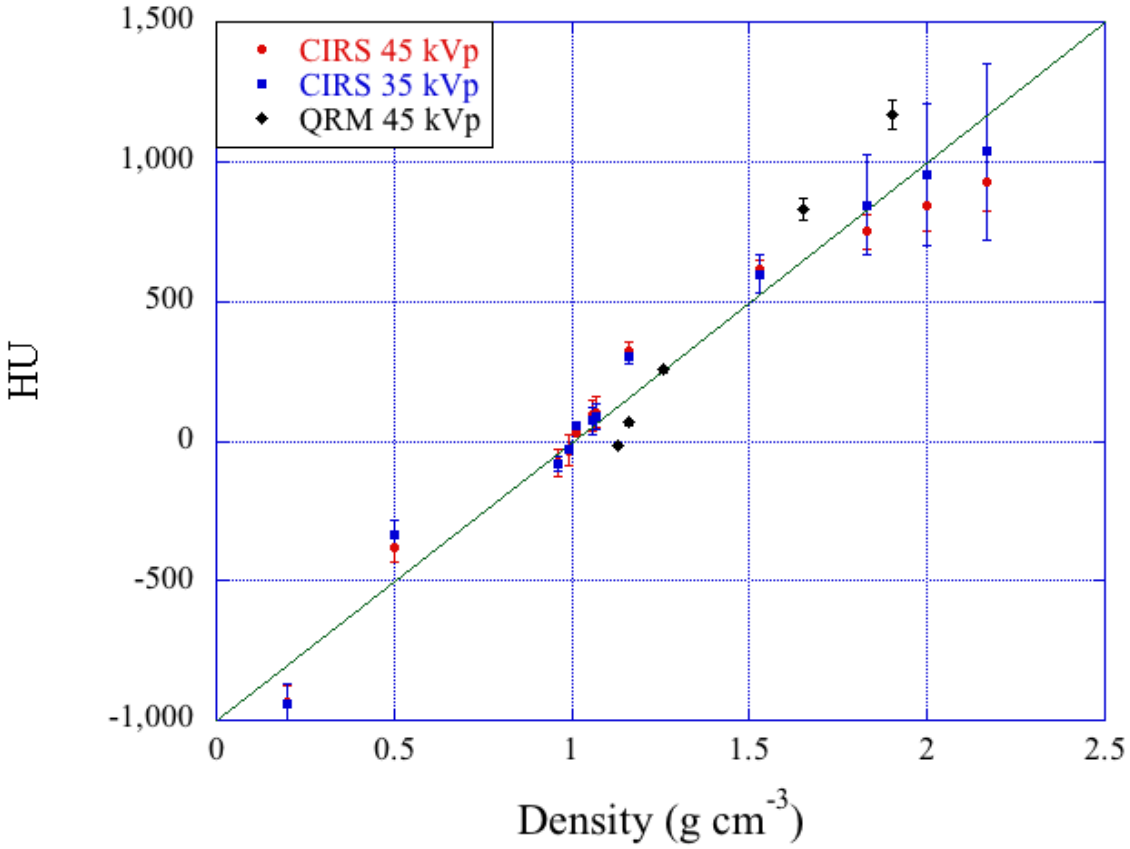

Figure 18. A plot of the measured HU values for the electron density plugs versus their density for the micro-CT.

It can be seen in the figure above that all of the data fall within range of the line except for the inhale, exhale, and trabecular bone. This is not the expected trend for these materials. Figure 19 shows the plot of the same electron density plugs measured in a clinical machine at 70 and 140 kVp.

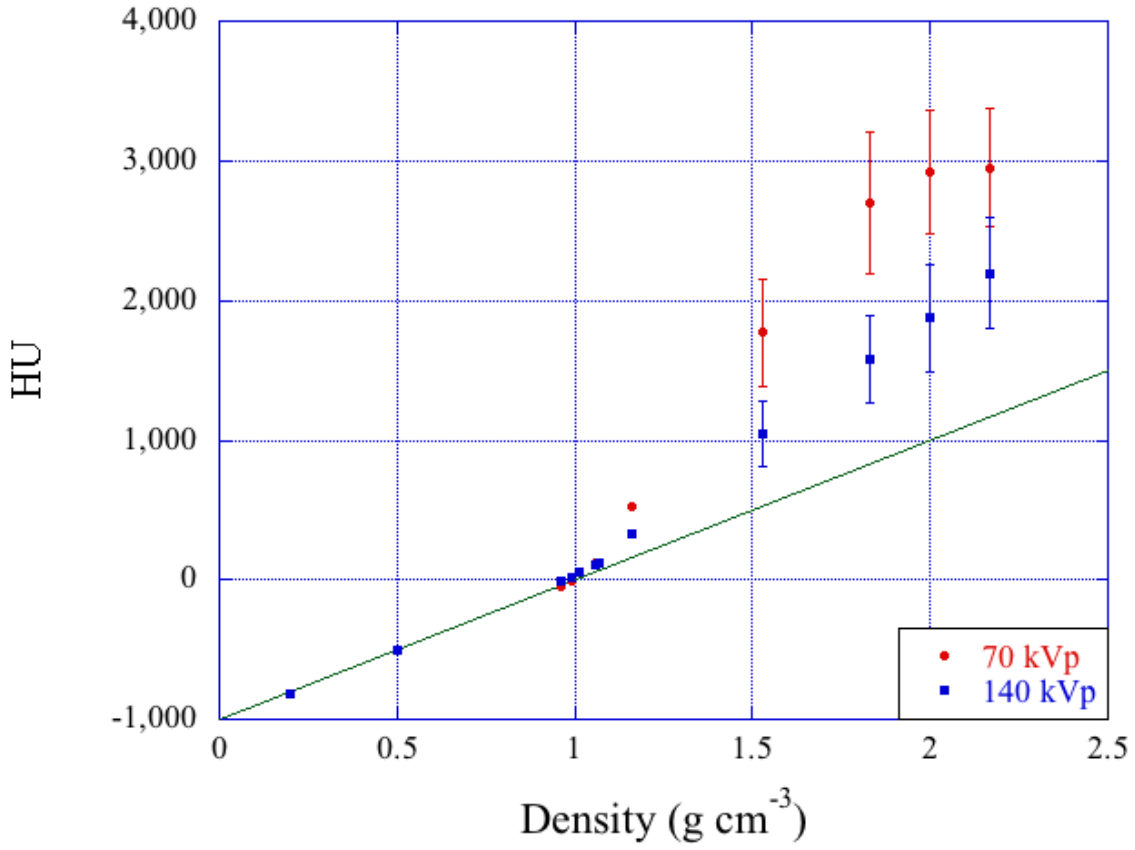

Figure 19. A plot of the same electron density plugs scanned on a Siemens Somatom 64 clinical CT machine.

This figure shows the expected trend, where in the region of bone, HU > 300, there is a greater rise in the HU value with the same change in density as there would be in the tissue region.

3.1.4 Electron Density Phantom Line Profiles

The single pixel line profiles for each tissue equivalent phantom are plotted in Figure 20 below. The images have been plotted only across the region of the image which contains the phantom while the imaging bed and air are not included in the plots. The amount of noise in the image along with the cupping artifact from the CBCT can easily be seen in sharp changes from one pixel to another and by the lower HU values in the center of the image compared to on the outer edges of the image. The statistics of each tissue equivalent plug are presented in Table 8.

From the plots and table, it can be seen that material differentiation is possible but in certain regions cannot be as precise as clinical CT machines. For example, in the range of tissues, -100 < HU < 150, muscle and liver tissues can be distinguished from adipose and breast tissues. However, since adipose and breast tissue ranges overlap each other, when looking to differentiate between each specific tissue type, a confident statement cannot be made about which material is being viewed. The same can be said for muscle and liver tissue, as well as dense bone at the outer regions of the plot.

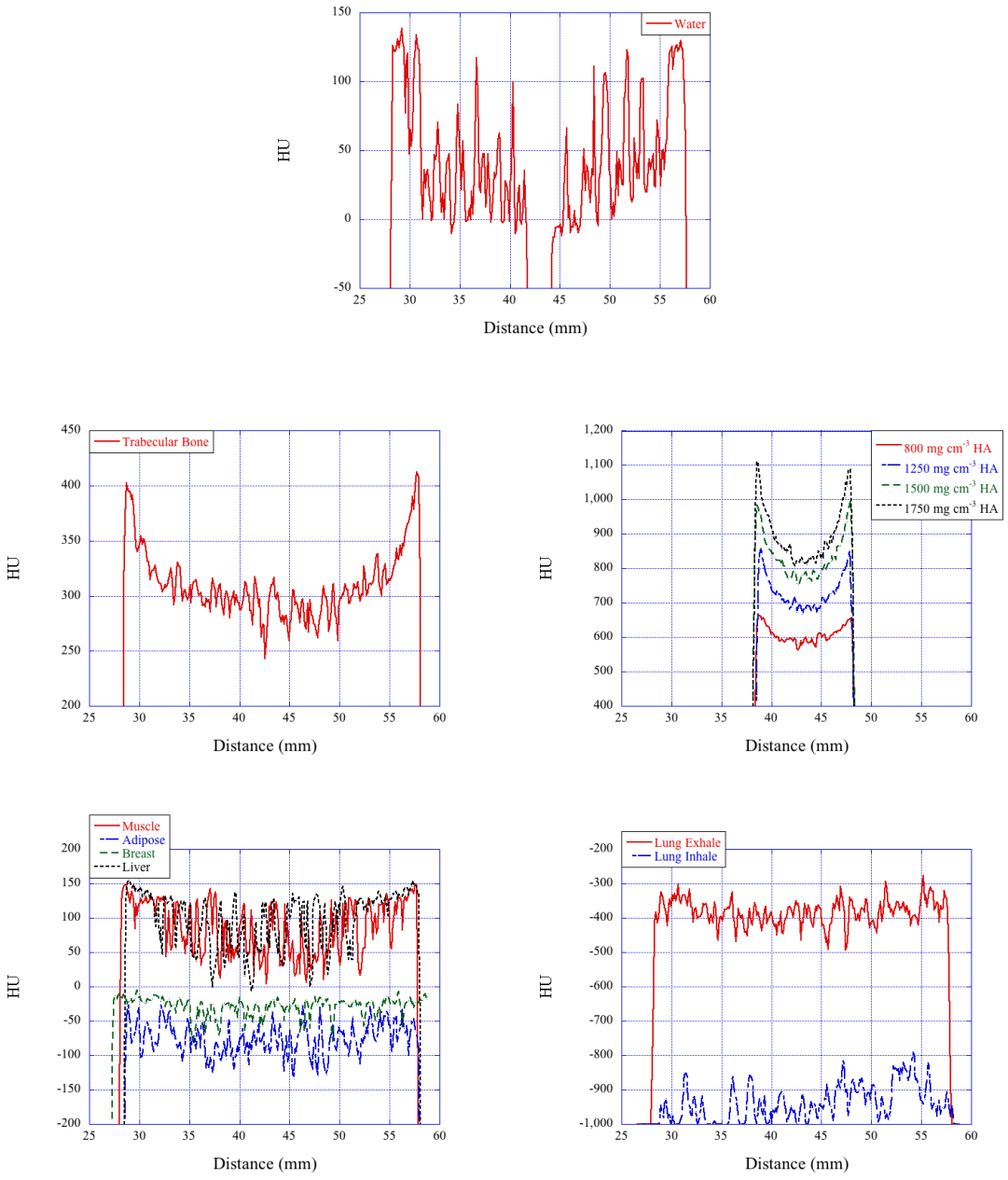

Figure 20. Single pixel line profiles through the CIRS phantom tissue equivalent plugs.

Table 8. Average, standard deviation, minimum, and maximum values for line profiles across each tissue equivalent phantom.

Tissue Equivalent	Average HU Value	Standard Deviation	Minimum HU Value	Maximum HU Value
Inhale	-937.79	52.15	-1000.00	-790.73
Exhale	-383.16	36.71	-493.18	-277.77
Adipose	-75.48	23.07	-134.34	-26.24
Breast	-28.69	13.97	-79.38	-4.85
Water	45.14	42.91	-13.14	138.49
Muscle	86.75	39.24	4.00	149.01
Liver	98.94	39.80	-6.53	155.28
Trabecular Bone	309.95	30.42	243.04	412.52
Dense Bone 800	595.60	61.67	261.99	663.50
Dense Bone 1250	706.07	108.95	201.64	857.04
Dense Bone 1500	810.61	117.36	293.05	998.73
Dense Bone 1750	870.86	149.46	245.59	1111.20

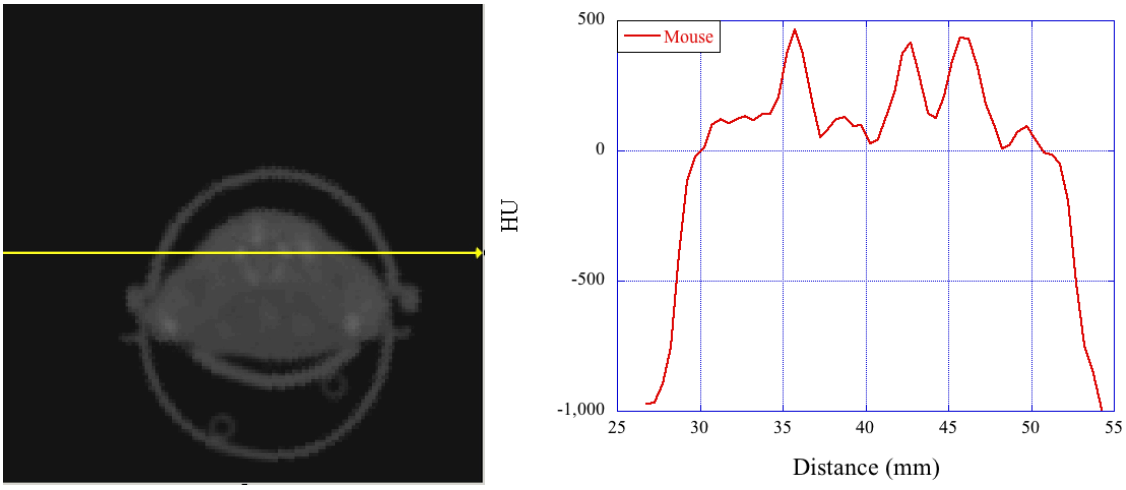

Figure 21. A single pixel line profile through a mouse subject.

Figure 21 shows a single pixel line profile, similar to those through the tissue equivalent phantoms, with the data plotted alongside the CBCT image. This line profile

runs across areas of both bone and tissue with HU values ranging from around 0 to approximately 500. While the noise levels and cupping artifacts appear to have a large effect in the tissue equivalent phantoms, it cannot readily be seen in the mouse line profile. This is true even when moving across different material boundaries. Further discussion on this topic will be covered in Section 4 below.

3.1.5 Theoretical HU Values as a Function of Material Composition

Using the photon energy spectrums, the material composition lists from ICRU, and the total linear attenuation coefficients obtained from NIST: XCOM an expected HU value can be calculated for each material. The results of this calculation are shown below in Table 9.

This table contains materials that should correspond to the tissue equivalent electron density plugs that are measured and discussed in the previous sub-section. These are the values that are expected from the measurements. Lung is expected to be in the region between exhale and inhale, trabecular bone should be similar to spongiosa and cortical bone should fall in the dense bone region between the 1.83 and 2.0 g cm^{-3} density plugs. Figure 22 shows the expected HU values plotted versus their density for both voltage potentials and a linear line which crosses through air at -1000 HU and water at 0 HU.

Table 9. ICRP tissues with the expected HU values calculated for each voltage of the micro-CT.

Tissue	ρ	n_0	Expected HU Value	
	kg m^{-3}	$m^{-3} \times 10^{26}$	35 kVp	45 kVp
Adipose tissue				
Adult #1	970	3240	-295.90	-279.33
Adult #2	950	3180	-352.72	-333.77
Adult #3	930	3120	-409.09	-387.80
Breast (whole)-50/50 (water/lipid)	960	3220	-248.70	-235.63
Liver				
Adult (healthy)	1060	3510	79.36	78.28
Adult (fatty)	1050	3480	35.72	36.74
Adult (cirrhotic)	1040	3450	-0.83	1.88
Lung				
Adult (healthy)	260	862	-733.98	-734.38
Adult (congested)	1040	3450	67.81	66.21
Muscle (skeletal)				
Adult	1050	3480	62.07	61.45
Skeleton-cortical bone				
Adult	1920	5950	8644.30	8224.56
Skeleton-spongiosa Adult	1180	3840	1588.81	1514.17
Water	1000	3340	0.00	0.00
Air	1.205		-1000.00	-1000.00

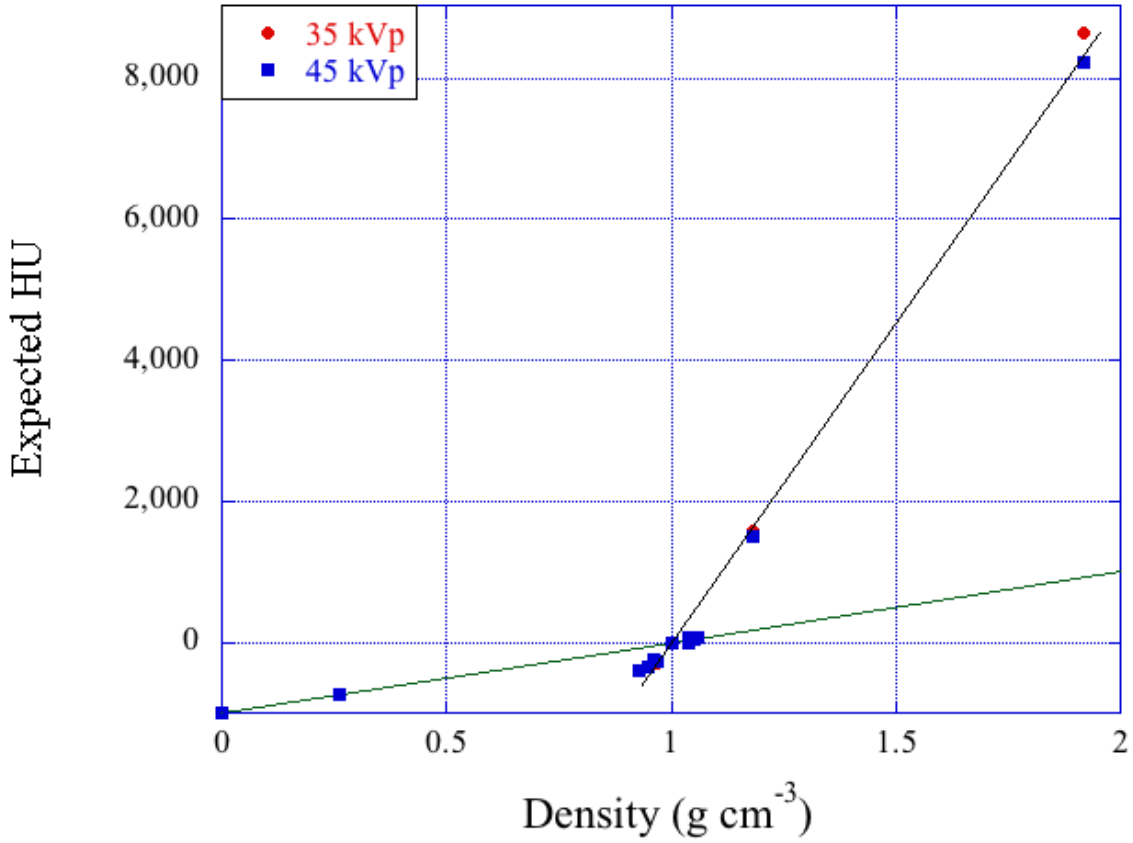

Figure 22. The expected HU values for the CIRS phantom plotted against their densities for voltage potentials of 34 and 45 kVp. A linear line is also plotted which passes through air at -1000 HU and water at 0 HU, and another through water at 0 HU and dense bone at ~8000 HU.

Comparing these values to expected values from an above subsection yields varying results. Since air is one of the calibration points for the machine, that value matches perfectly. Lung, muscle, and liver all fall within error of their calculated values from ICRU. Adipose, breast, and bone are well outside the error ranges for their corresponding materials from ICRU. Using the equation for calculating the HU value

and using the linear attenuation coefficient for bone at different energies it was determined that the effective energy which would have yielded correct results was above 140 keV. For an x-ray machine with a maximum operating voltage potential of 50 kVp this is not possible. It was concluded that the CT subsystem uses a calibration which causes the bone to fall on the same linear trend line as the region between air and water, which for clinical CT scanners is not the case.

3.1.6 Nominal Absorbed Dose per CBCT Scan

Using the water phantom and the PTW ionization chamber described before, the surface and deep absorbed dose were estimated for the 45 kVp setting. The results for both the superficial- and deep-dose equivalent measurements at low and high current settings and high voltage are shown in Figure 23 and Figure 24 below.

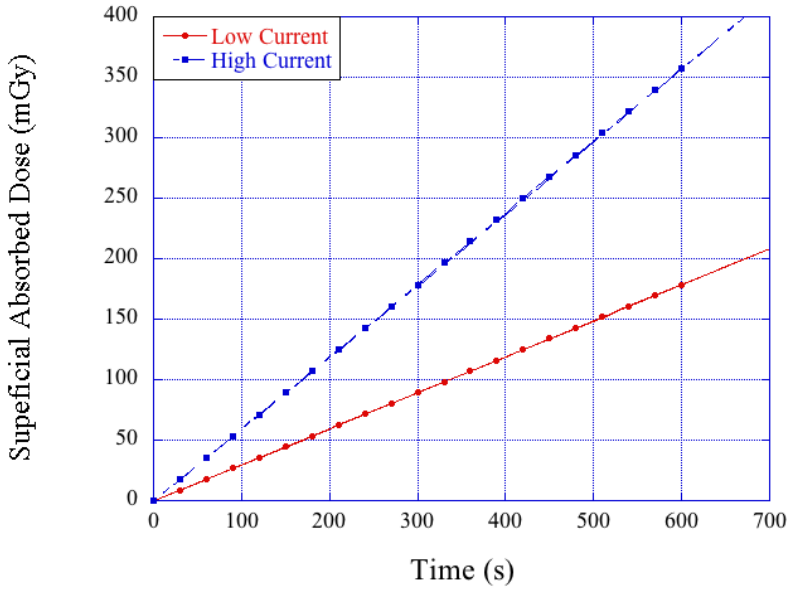

Figure 23. The superficial-dose equivalent over time for a low and high current scan at the highest voltage setting. The slopes for the linear fits are 0.2979 mGy s^{-1} for the low current and 0.5957 mGy s^{-1} for the high current. Both y-intercepts are 0.

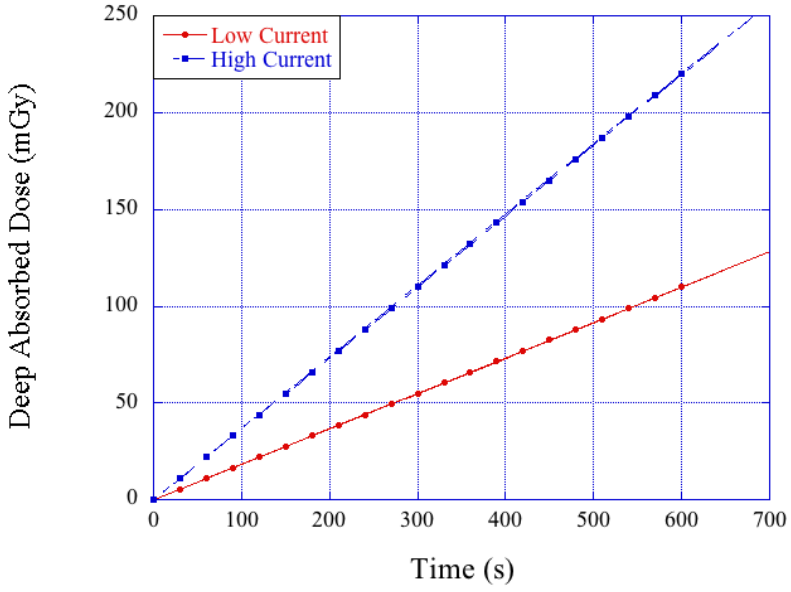

Figure 24. The deep absorbed dose equivalent over time for a low and high current scan at the highest voltage setting. The slopes for the linear fits are 0.1833 mGy s^{-1} for the low current and 0.3667 mGy s^{-1} for the high current. Both y-intercepts are 0.

Using the linear trend lines fit to the data the total dose can be calculated for each type of scan, as long as the scanning time is known. These values are shown in Table 10 and can be used during longitudinal studies to track the dose received for each animal over the multiple scan sessions.

Table 10. The superficial- and deep-dose equivalent vales for low and high current settings at the maximum voltage, 45 kVp.

	Superficial Dose Equivalent (mGy)		Deep Dose Equivalent (mGy)	
	Low Current	High Current	Low Current	High Current
Standard (3 min)	53.6	107.2	33.0	66.0
Good (5 min)	89.4	178.7	55.0	110.0
Best (8 min)	143.0	285.9	88.0	176.0
High Resolution (10 min)	178.7	357.4	110.0	220.0

If there was a longitudinal study that required a total of five scans, at the lowest setting of resolution, 500 μm, and current, the total superficial dose would be 0.268 Gy and the deep dose would be 0.165 Gy.

3.2 Positron Emission Tomography

The PET unit was used to measure the calibration and uncertainties of the machine along with the partial volume effects. The results of the studies are discussed in the following subsections.

3.2.1 Calibration and Uncertainties

The calibration of the micro-PET requires a uniformity phantom based on a cylinder. Figure 25 shows an image of the resulting long uniformity phantom (99 ml) used for calibration purposes. The images show uniform distribution over the whole phantom with minimal uncertainties, which were quantitated for calibration purposes. Acquisitions were obtained at different time points to assess the uniformity and response as a function of activity concentration. The region of interest (in pink) in the image corresponds to that analyzed for establishing the Q value of the system. No significant variations were observed as a function of RIO size.

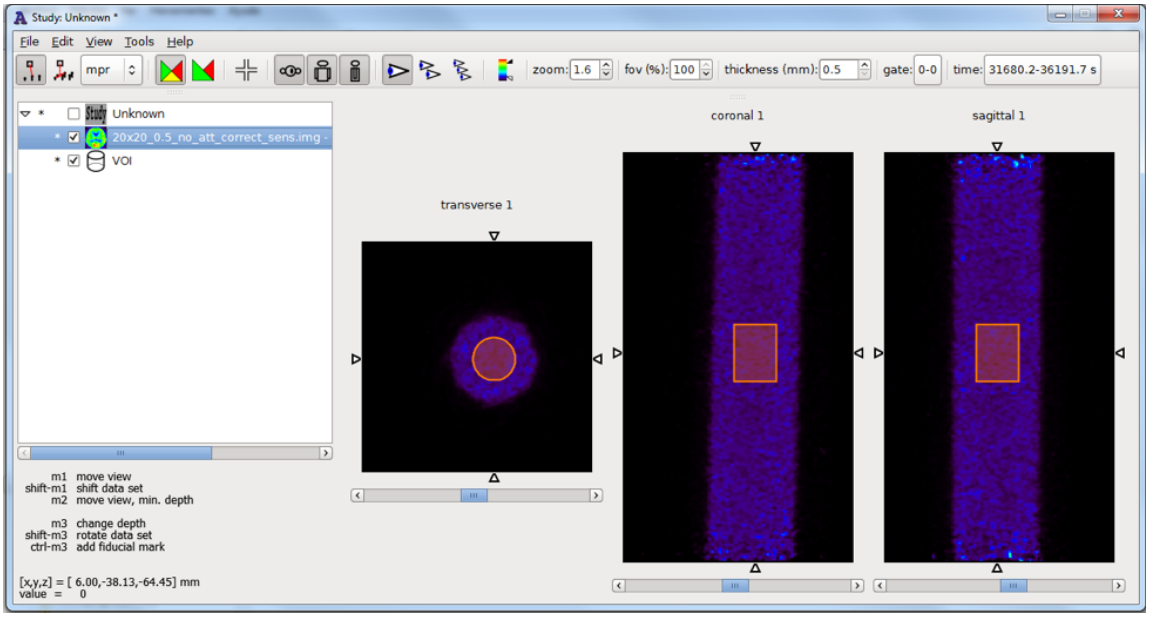

Figure 25. Long uniformity phantom used to assess the Q value for the micro-PET system.

The initial activity in the phantom was 45473 ± 909 kBq at the time of calibration. Once the phantom is in the system, it calculates the activity at the corresponding elapsed time of image acquisition from calibration time for every frame and provides the corresponding activity concentration at midpoint. The duration of each scan was 300 s and the midpoint of each scan was 150 s. The Q value is then calculated by inspecting the data for linearity, selecting the range of data (activity concentrations) where the system is linear, and using linear regression analysis, assess the corresponding Q value and corresponding uncertainty. The Q value of the system needs to be under quality control based on quality assurance standards that indicate that the systems is stable when the variations within calibrations (QC) do not deviate from 5%.

The resulting values are presented in Table 11 and are plotted in Figure 26 with a linear trend line between counts per unit volume and activity concentration. Three different regions can be observed including regions of saturation, under response, and supra-linearity. The micro-PET system was found to be linear for activity concentration below 25 kBq/ml with a saturation limit of 100 kBq/ml. Therefore, the micro-PET subsystem can only be considered to be quantitative when total activities are less than the saturation limit of 7.4 MBq (200 μCi).

Table 11. Data obtained for multiple frames used to calculate the Q value of the micro-PET system.

Frame	Time (s)	Mean Counts	Standard Deviation	Concentration (kBq/ml)	Standard Deviation
0	5010	1.71×10^{-3}	4.10×10^{-4}	271.140	65.10
1	7110	9.91×10^{-4}	1.45×10^{-4}	217.388	31.78
2	9210	1.02×10^{-3}	1.20×10^{-4}	174.293	20.53
3	11310	1.13×10^{-3}	1.14×10^{-4}	139.741	14.05
4	13410	1.16×10^{-3}	1.14×10^{-4}	112.038	10.97
5	15510	1.11×10^{-3}	1.09×10^{-4}	89.828	8.82
6	17610	1.02×10^{-3}	1.03×10^{-4}	72.020	7.33
7	19710	9.01×10^{-4}	9.82×10^{-5}	57.743	6.29
8	21810	7.69×10^{-4}	8.90×10^{-5}	46.296	5.36
9	23910	6.49×10^{-4}	8.04×10^{-5}	37.118	4.60
10	26010	5.36×10^{-4}	7.47×10^{-5}	29.760	4.15
11	28110	4.43×10^{-4}	6.75×10^{-5}	23.860	3.64
12	30210	3.61×10^{-4}	6.03×10^{-5}	19.130	3.19
13	32310	2.96×10^{-4}	5.49×10^{-5}	15.338	2.85
14	34410	2.39×10^{-4}	4.84×10^{-5}	12.297	2.49
15	36510	1.92×10^{-4}	4.34×10^{-5}	9.859	2.22
16	38610	1.55×10^{-4}	3.96×10^{-5}	7.905	2.02
17	40710	1.26×10^{-4}	3.61×10^{-5}	6.338	1.82
18	42810	1.00×10^{-4}	3.30×10^{-5}	5.081	1.68
19	44910	8.05×10^{-5}	2.92×10^{-5}	4.074	1.48

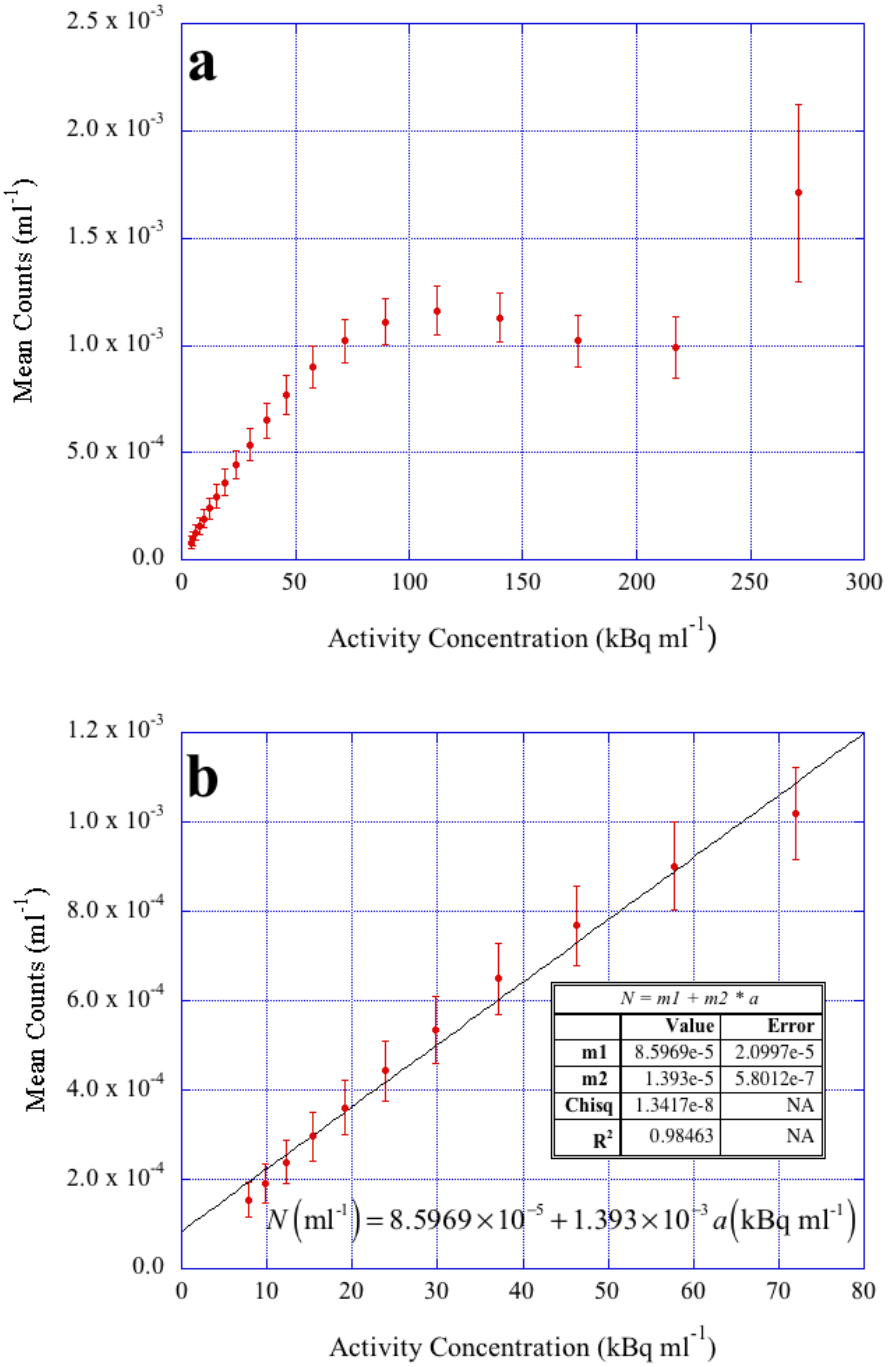

Figure 26. Performance characteristics of the Albira micro-PET showing the mean count per unit volume as a function of activity concentration. The response is not linear at activity concentration higher than 50 kBq ml^{-1}, showing a saturation activity concentration about 80 kBq/ml, the system becomes supra linear at activity concentration higher than 250 kBq ml^{-1}.

3.2.2 Resolution

The spatial resolution of the micro-PET system was estimated using a modified Derenzo phantom where the activity, acquisition time and MLEM iterations were tested. The diameters of the hot rods of the modified Derenzo phantom were 0.75, 1.0, 1.35, 1.70, 2.0, and 2.4 mm. Figure 27 and Figure 28 show the transaxial images of the Derenzo phantom where the best resolution was 0.75 mm using a minimum of 100 iterations.

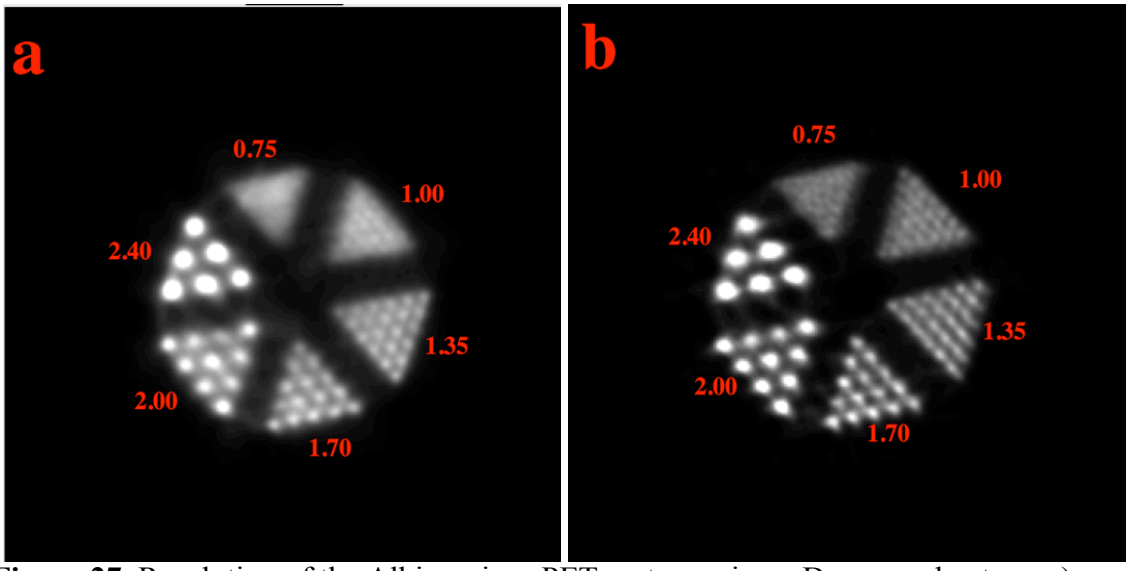

Figure 27. Resolution of the Albira micro-PET system using a Derenzo phantom. a) Acquisition time: 5 min, 17760 kBq (480 μCi), MLEM: 12 iterations, voxel size 0.4 mm. b) Acquisition time: 2 h, activity 10767 kBq (291 μCi), MLEM: 120 iterations, voxel size 0.4 mm.

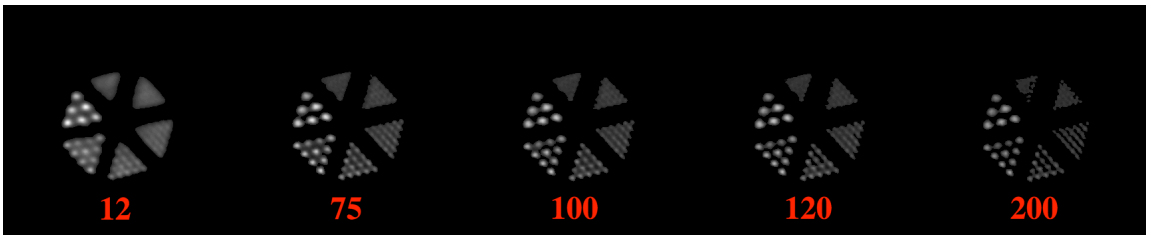

Figure 28. Resolution of the Albira micro-PET system using a Derenzo phantom at different iteration levels. Acquisition time: 2 h. Activity 10767 kBq (291 μCi), voxel size 0.4 mm.

It can be seen from Figure 27 that having a higher total activity concentration does not assure a better resolution, as there will be more artifacts associated with sensitivity, scatter and random counts. Lower activity and a higher number of iterations (longer reconstruction times) provides better resolution and lower partial volume effects.

3.3 micro-CT and micro-PET Image Registration and Uncertainty

After individual quantification of each machine, the micro-PET/CT unit was used to measure the co-registration and uncertainty of the individual imaging modality images. The co-registered image of the CBCT and the PET from the cross-capillary study and the single pixel line profile comparison of the two units are shown in Figure 29 and Figure 30 below.

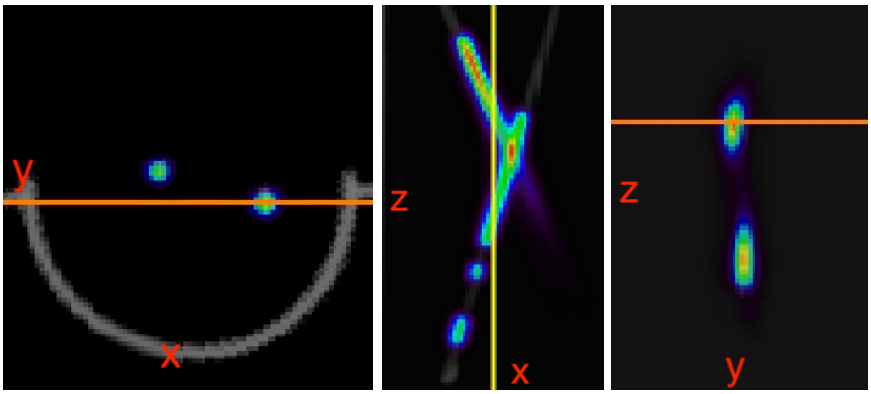

Figure 29. Single pixel line profile through cross capillaries used to assess the Δx, Δy, and Δz displacement to attain co-registration of PET and CT images.

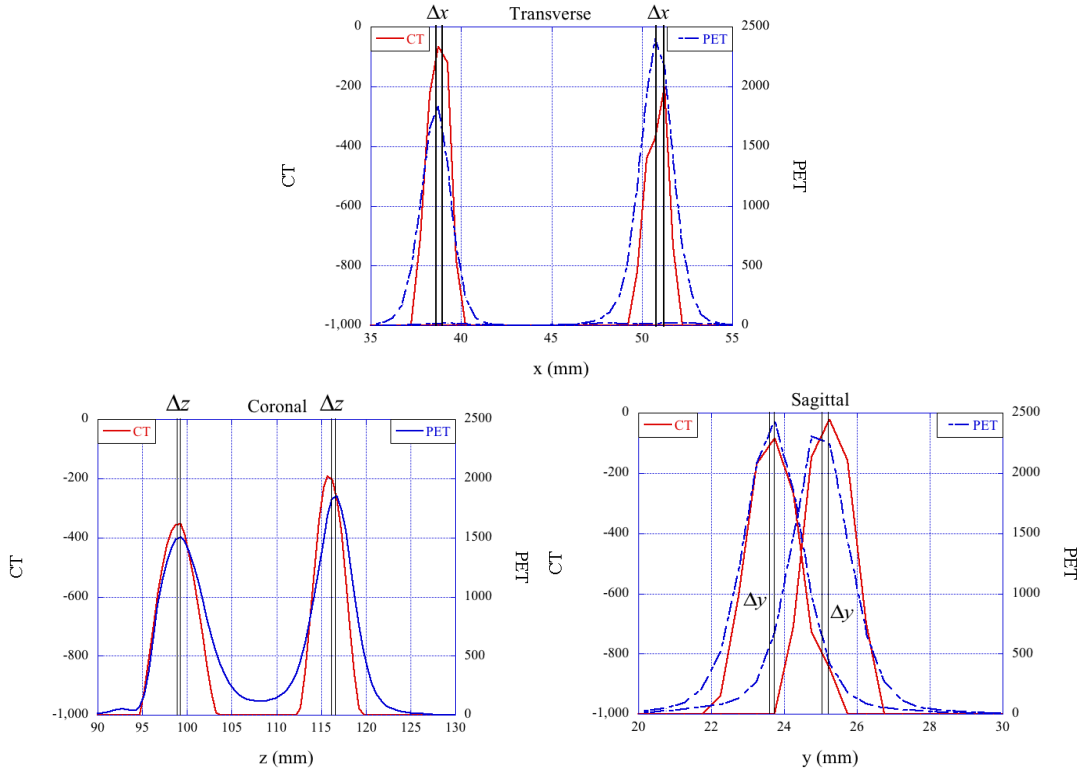

Figure 30. Single pixel line profiles for both the PET and CT images for the assessment of Δx, Δy, and Δz displacement using the cross-capillaries study. A cubic spline function was used to determine the maximum peaks for the different line profiles.

It can easily be seen that the PET and CT images give different ranges for the size and position of the capillaries in the image. This particular line was chosen because it crossed the capillaries at multiple locations in the same line. Since the line is so close to the center cross of the capillaries, the PET values never return to zero even though the line crosses through a collection of air before crossing another capillary. A distribution of PET tracer can also be seen in the first capillary crossing where there are two peaks in a location only one would be expected. This is due to improper filling of the capillaries with the PET tracer. While the peaks do not line up exactly, when considering only values above 1% of the total counts in the PET line profile, the peaks of the PET and CT fall within an acceptable range. The displacement was estimated as the average of at least two points given their minimum and maximum values. In the *x* axis the displacement was estimated at 0.405 mm (0.39 mm – 0.42 mm), in the *z* axis was estimated at 0.21 mm (0.19 mm – 0.23 mm), and in the *y* axis was 0.15 mm (0.14 mm – 0.16 mm). These displacement values are provided into the header of the images to attain co-registration when the images are superimposed. There is no rotation algorithm at the present moment as it is assumed that the z axis corresponding to the table movement is linear. However, we have noticed that the weight of the animal does affect the coronal plane due to a significant tension on the bed as it moves inside the CT unit. To correct for this potential issue a study cradle for the animal bed is currently being design.

3.4 Computational Assessment of Subject Absorbed Dose

As described above, two studies were run in MCNP to calculate the dose per voxel for both [^{18}F]FDG and [^{18}F]NaF.

Table 12. A breakdown of the division of HU values into material bins with the composition and density give. These divisions are used to divide the CT values into materials for use in the MCNP program.

MCNP Material Number	HU Range (min, max)	ρ (g cm^{-3})	Composition											
			H	C	N	O	Na	Mg	P	S	Cl	Ar	K	Ca
1	-1000, -950	0.00121			75.5	23.2						1.3		
2	-950, -125	0.48	10.3	10.5	3.1	74.9	0.2		0.2	0.3	0.3		0.2	
3	-125, -90	0.93	11.6	68.1	0.2	19.8	0.1			0.1	0.1			
4	-90, -55	0.96	11.3	56.7	0.9	30.8	0.1			0.1	0.1			
5	-55, 0	0.98	11	45.8	1.5	41.1	0.1		0.1	0.2	0.2			
6	0, 50	1.01	10.8	35.6	2.2	50.9			0.1	0.2	0.2			
7	50, 65	1.03	10.6	28.4	2.6	57.8			0.1	0.2	0.2		0.1	
8	65, 120	1.06	10.3	13.4	3	72.3	0.2		0.2	0.2	0.2		0.2	
9	120, 180	1.09	9.4	20.7	6.2	62.2	0.6			0.6	0.3			
10	180, 270	1.11	9.5	45.5	2.5	35.5	0.1		2.1	0.1	0.1		0.1	4.5
11	270, 340	1.17	8.9	42.3	2.7	36.3	0.1		3	0.1	0.1		0.1	6.4
12	340, 380	1.22	8.2	39.1	2.9	37.2	0.1		3.9	0.1	0.1		0.1	8.3
13	380, 415	1.28	7.6	36.1	3	38	0.1	0.1	4.7	0.2	0.1			10.1
14	415, 450	1.34	7.1	33.5	3.2	38.7	0.1	0.1	5.4	0.2				11.7
15	450, 485	1.40	6.6	31	3.3	39.4	0.1	0.1	6.1	0.2				13.2
16	485, 520	1.46	6.1	28.7	3.5	40	0.1	0.1	6.7	0.2				14.6
17	520, 555	1.52	5.6	26.5	3.6	40.5	0.1	0.2	7.3	0.3				15.9
18	555, 590	1.58	5.2	24.6	3.7	41.1	0.1	0.2	7.8	0.3				17
19	590, 625	1.64	4.9	22.7	3.8	41.6	0.1	0.2	8.3	0.3				18.1
20	625, 660	1.70	4.5	21	3.9	42	0.1	0.2	8.8	0.3				19.2
21	660, 695	1.76	4.2	19.4	4	42.5	0.1	0.2	9.2	0.3				20.1
22	695, 730	1.82	3.9	17.9	4.1	42.9	0.1	0.2	9.6	0.3				21
23	730, 765	1.88	3.6	16.5	4.2	43.2	0.1	0.2	10	0.3				21.9
24	> 765	1.93	3.4	15.5	4.2	43.5	0.1	0.2	10.3	0.3				22.5

To begin, the respective CT images were read in and their HU values were used to create an array containing the MCNP material number for each voxel location. Table 12 gives the HU range, density, and material composition in weight percent for each of the 24 different materials used in MCNP.

3.4.1 [^{18}F]FDG Study

The first study was a [^{18}F]FDG retro-orbital injection of 9997.4 kBq (270.2 μCi). The mouse was anesthetized using isoflurane for the for the retro-orbital injection, then allowed to wake up and become alert for approximately an hour before it was put to anesthetized again for subsequent imaging. The time of active wakefulness allowed the [^{18}F]FDG to distribute throughout the different organs of the body and subsequent uptake in sites of high metabolic activity. The CT was set for a standard image with a scan time of approximately 3 min while the PET scan time was 60 min.

Figure 31 shows the micro-CT image acquired during this study. The micro-PET/CT system saves the images files using the Analyze format, which were subsequently converted into DICOM format. These files were then read by the python code creating a new array containing the material number for each voxel. This material array was further converted into a DICOM format for comparison purposes and is shown in Figure 32.

Figure 31. Slice image of the micro-CT for the animal study using [^{18}F]FDG.

The CT and material images should appear similar with the exception that an HU range from -1000 to approximately 2000 is condensed to a range from 1 to 24 in the material image.

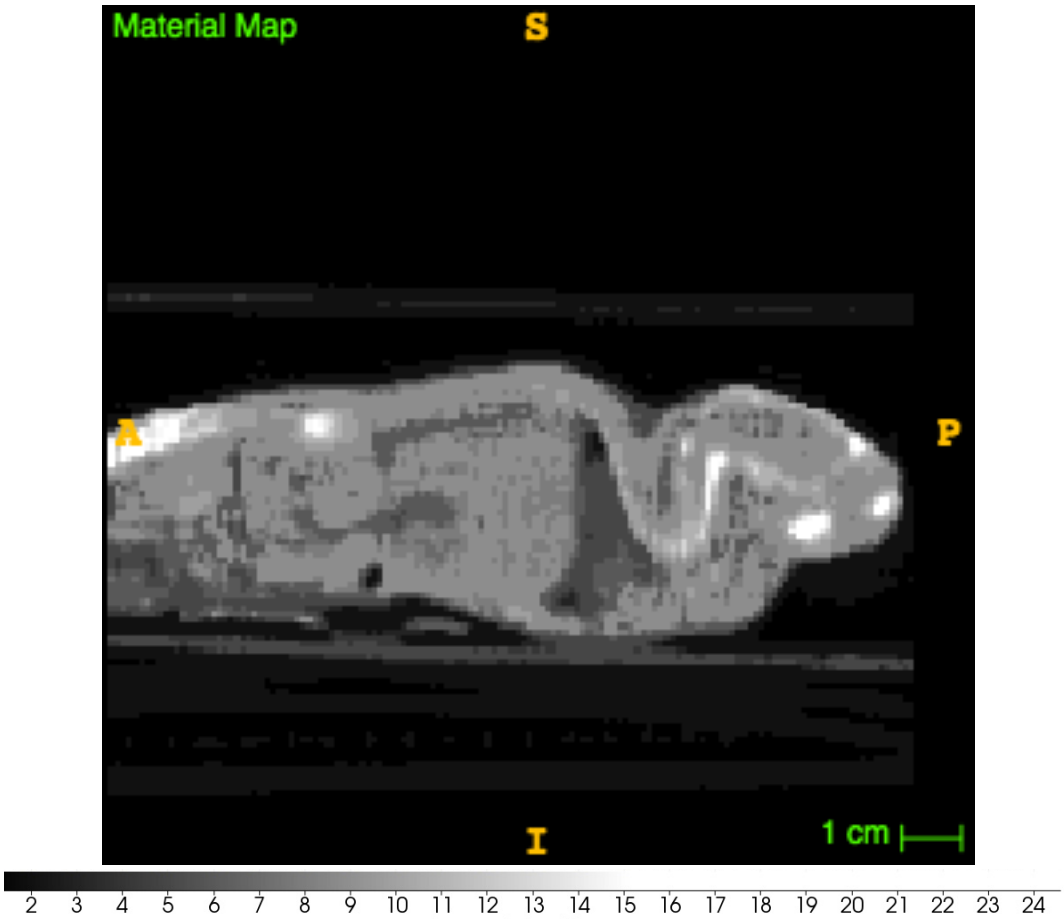

Figure 32. Slice image of the material values used in MCNP for the animal study using [^{18}F]FDG.

After the material array is created, the PET images from the study are read in to create the source term for the MCNP input deck. The PET images are shown in Figure 33 below. A large concentration can be seen in the eye socket where the injection occurred, bladder, kidney and brain. These are areas where higher radiation doses are expected in the MCNP output.

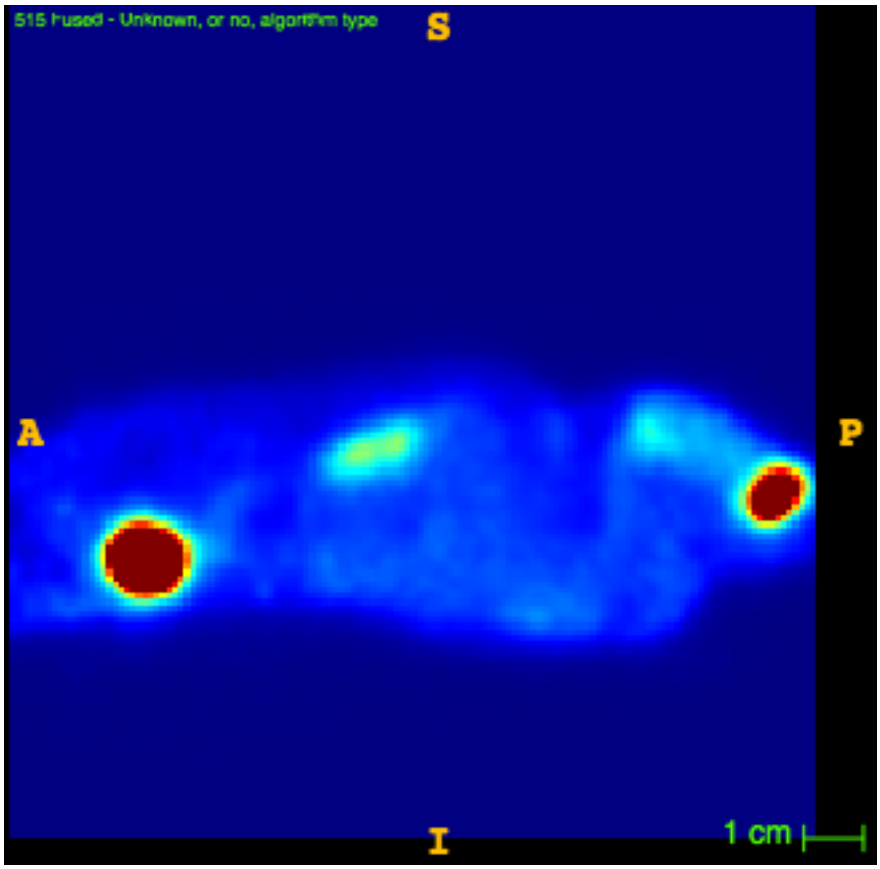

Figure 33. Slice image of the co-registered micro-PET and micro-CT for the animal study using [^{18}F]FDG.

With all of these as input the program was executed and ran for 10^7 particles and the MCNP results in text format were converted again into DICOM format. Figure 34 shows the voxel absorbed dose results co-registered with the original CT while Figure 35 shows the relative error of the voxel dose.

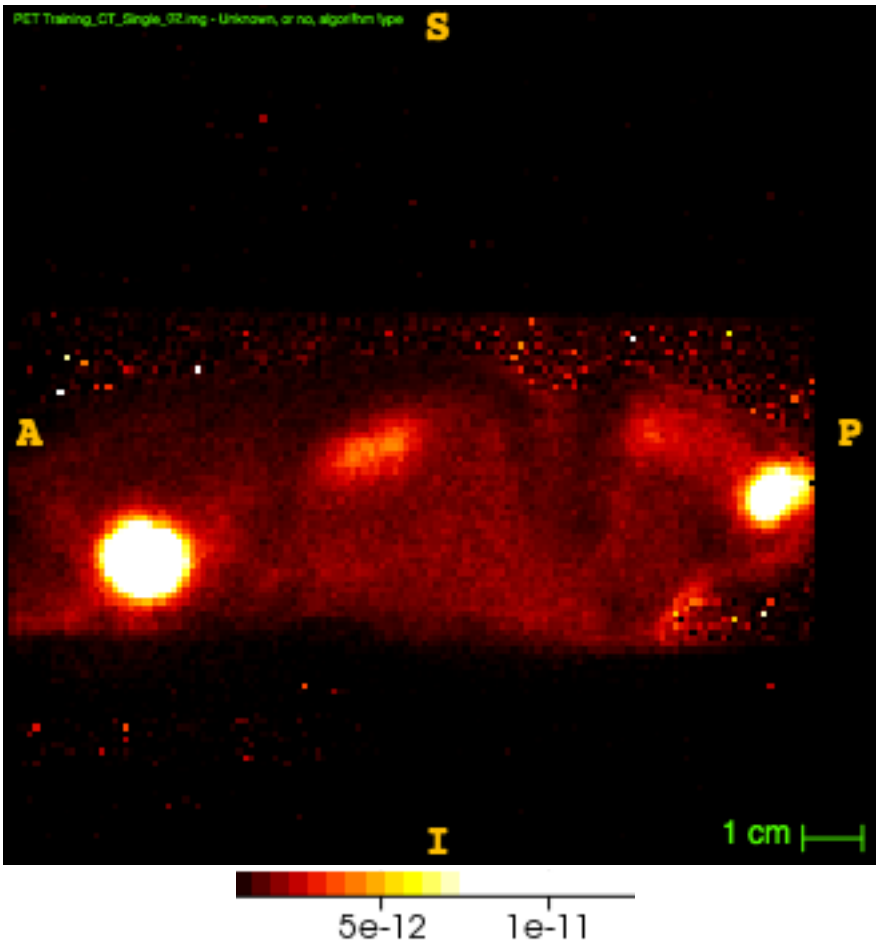

Figure 34. Slice image of the co-registered dose and micro-CT for the animal study using [^{18}F]FDG.

At first glance, Figure 34 looks as expected, with the lowest dose areas occurring outside of the animal in the air and highest dose areas occurring in the animal around the PET source locations. The scale is in units of Gy Bq^{-1} s^{-1}, so the total dose to any voxel needs to be multiplied by the total number of disintegrations that are occurring in the body.

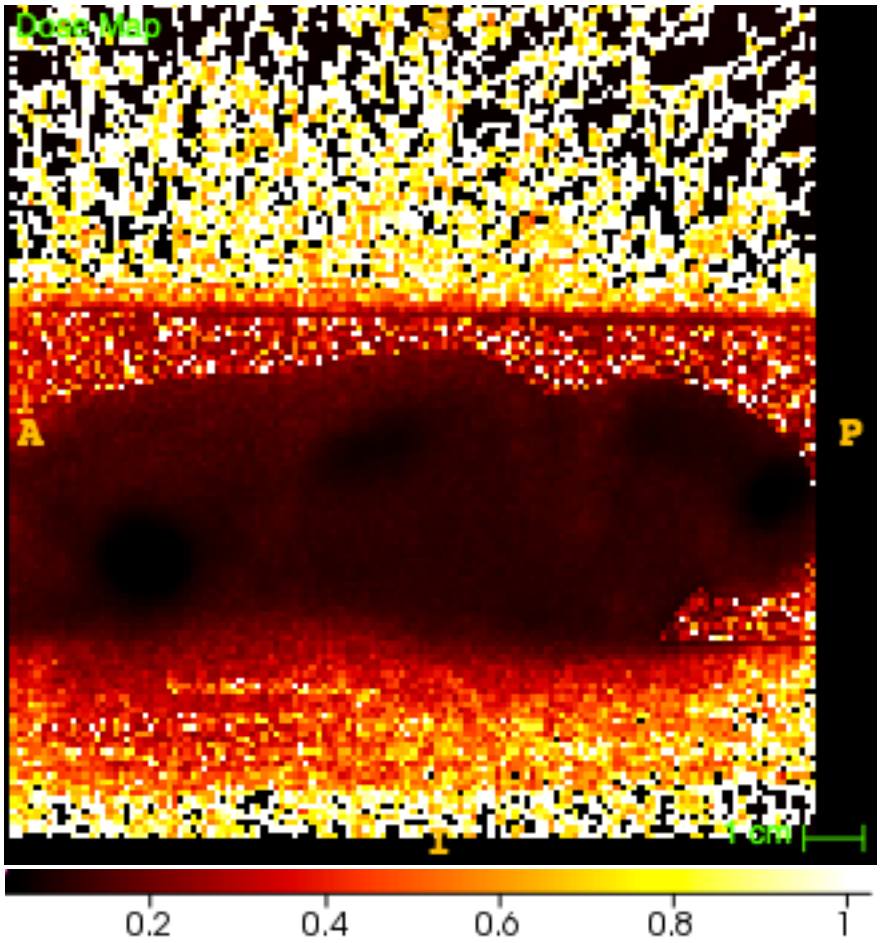

Figure 35. Slice image of the co-registered dose relative error and micro-CT for the animal study using [^{18}F]FDG.

The relative error was calculated for the dose at each voxel. Most locations inside on the animal have a relative error below 0.10, while regions further away from the PET tracer location, like air, have higher relative uncertainties and the streaming effects of the created pair production photons can be seen. Continuing to run more particles will decrease the relative errors even further, but locations outside of the animal are not of

interest so as long as the relative doses inside the subject are below 20% it is not deemed necessary.

Rough segmentation was done on the images to determine mean absorbed dose values to potential organs of interest. Figure 36 shows the segmentation labels on top of the micro-CT slices as well as a 3D image of the regions in the bottom right corner. Table 13 gives the mean absorbed dose values for each region along with their standard deviation.

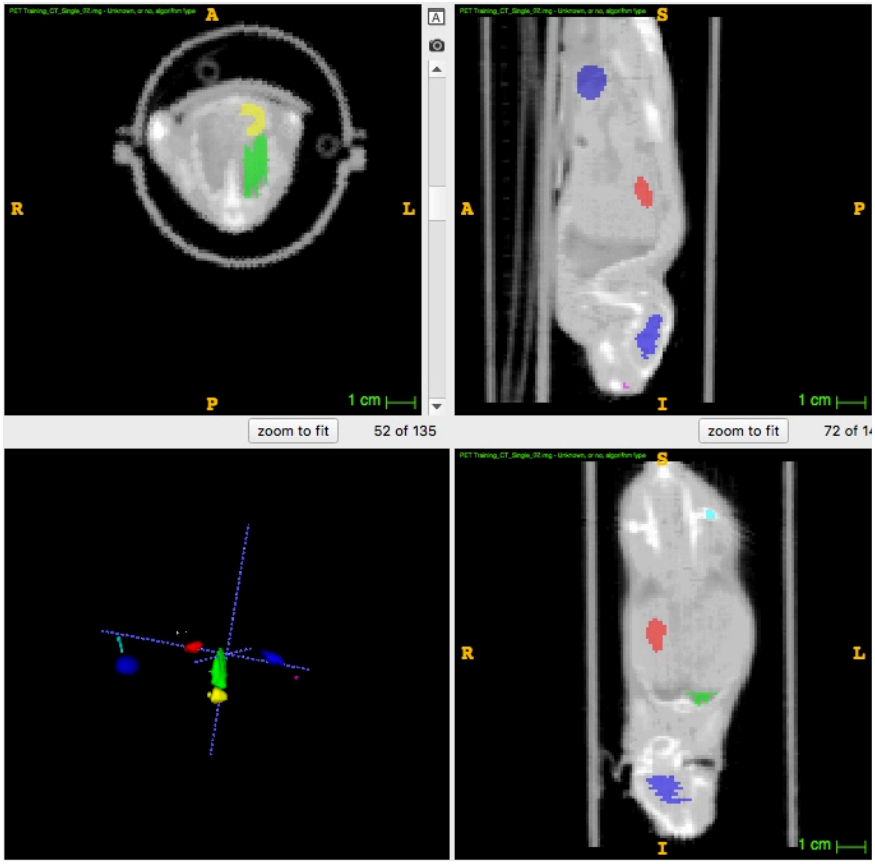

Figure 36. Segmentation performed in ITK-SNAP provided mean values for the absorbed dose in different potential organs of interest for the animal study using [^{18}F]FDG. Kidney is marked in red, Lung in green, Brain in blue, Heart in yellow, Bone – Femur in neon blue, Eye in pink, Bone – Spine in khaki, and Bladder in dark blue.

Table 13. Absorbed dose estimates of [^{18}F]FDG for different target regions. The regions were delineated using the micro-CT images in ITK-SNAP.

Tissue	Absorbed Dose (Gy Bq^{-1} s^{-1})	Relative Error
Kidney	3.86×10^{-12}	0.065
Lung	1.64×10^{-12}	0.103
Brain	2.19×10^{-12}	0.086
Heart	4.45×10^{-12}	0.060
Bone - Femur	5.88×10^{-13}	0.161
Eye	1.48×10^{-11}	0.034
Bone - Spine	7.98×10^{-13}	0.141
Bladder	4.02×10^{-11}	0.026
Whole Body	1.48×10^{-12}	0.137

While the values in Table 13 come from a quick segmentation process they show some generally expected trends based on the distribution of the PET tracer used. For example, the eye and bladder, the two hottest locations on the PET image, have the highest absorbed dose values. The kidney, brain, and heart receive the moderate absorbed dose values and are also where our hotter spots were in Figure 33. Lower doses were seen in areas with less PET counts like the bones and lungs.

3.4.2 NaF Study

The second study conducted was a tail vein injection of [^{18}F]NaF with an activity of 5379.8 kBq (145.4 μCi). The CT was set for a standard image with a scan time of approximately 3 min while the PET scan time was 60 min. The CT images are presented in Figure 37 and are used to begin to create the MCNP input deck.

The CT image is again taken and remapped from a range of -1000 to above 3000 HU into twenty-four different material bins based on the HU value. The material images are shown in Figure 38 and are in good agreement with the CT images. The bone PET tracer serves as a minor contrast agent for the CT allowing the bones to be viewed more easily. Because of this, the tissue materials appear darker in this study than they did in the previous [^{18}F]FDG study.

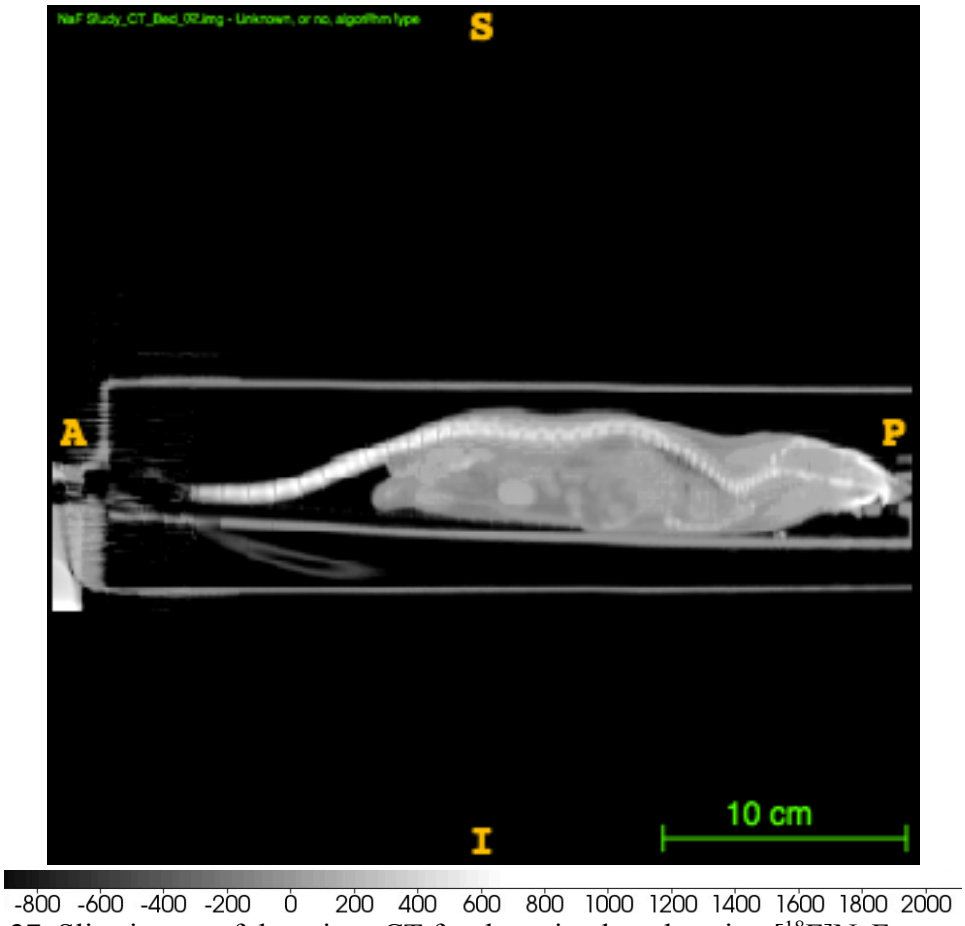

Figure 37. Slice image of the micro-CT for the animal study using [^{18}F]NaF.

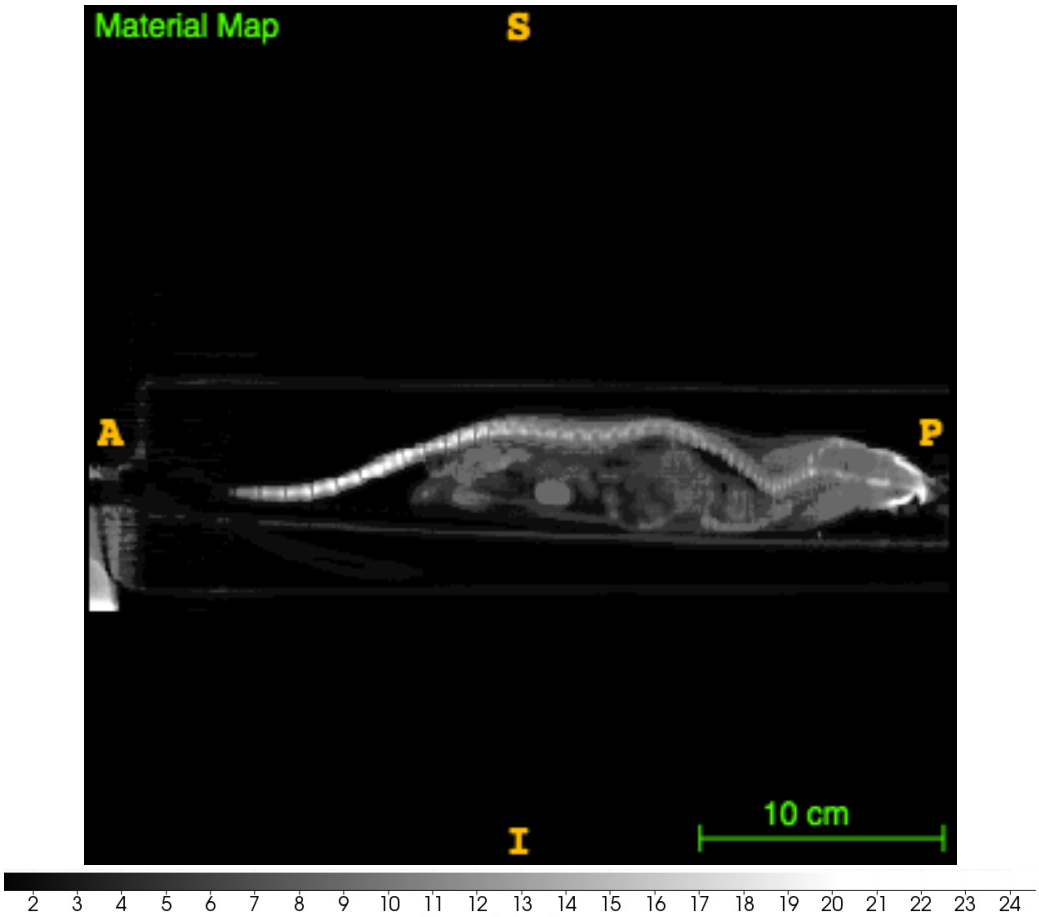

Figure 38. Slice image of the material values used in MCNP for the animal study using [^{18}F]NaF.

The PET images for this study are shown in Figure 39 below. Since the tracer [^{18}F]NaF seeks out bone, the PET image is expected to highlight the bone regions, which it does. The spinal cord, ribs, and skull are all clearly visible in the PET image below and are areas where higher radiation doses are expected in the MCNP output.

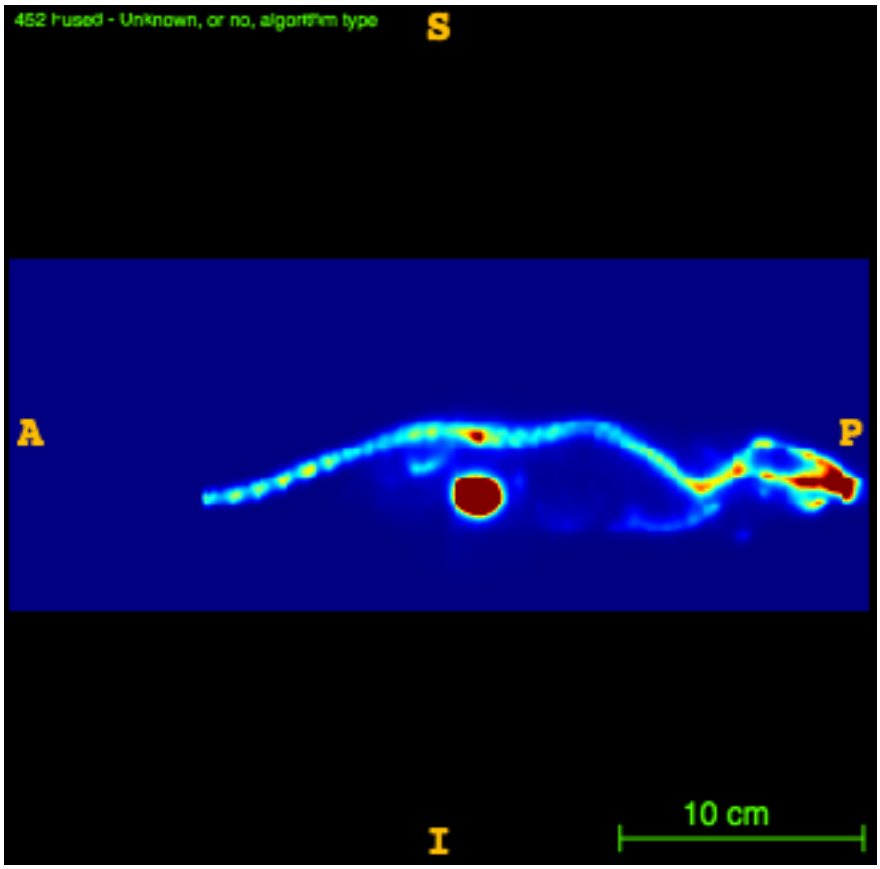

Figure 39. Slice image of the co-registered micro-PET and micro-CT for the animal study using [^{18}F]NaF.

With all of these as input, the program was run for 1.5×10^7 particles and the results were converted to the DICOM format. The relative error values were higher in this study due to the more localized source. To counter this effect, more particles than the previous study were run to achieve relative error values on a similar scale. Figure 40 shows the voxel dose results co-registered with the original CT while Figure 41 shows the relative error of the voxel dose.

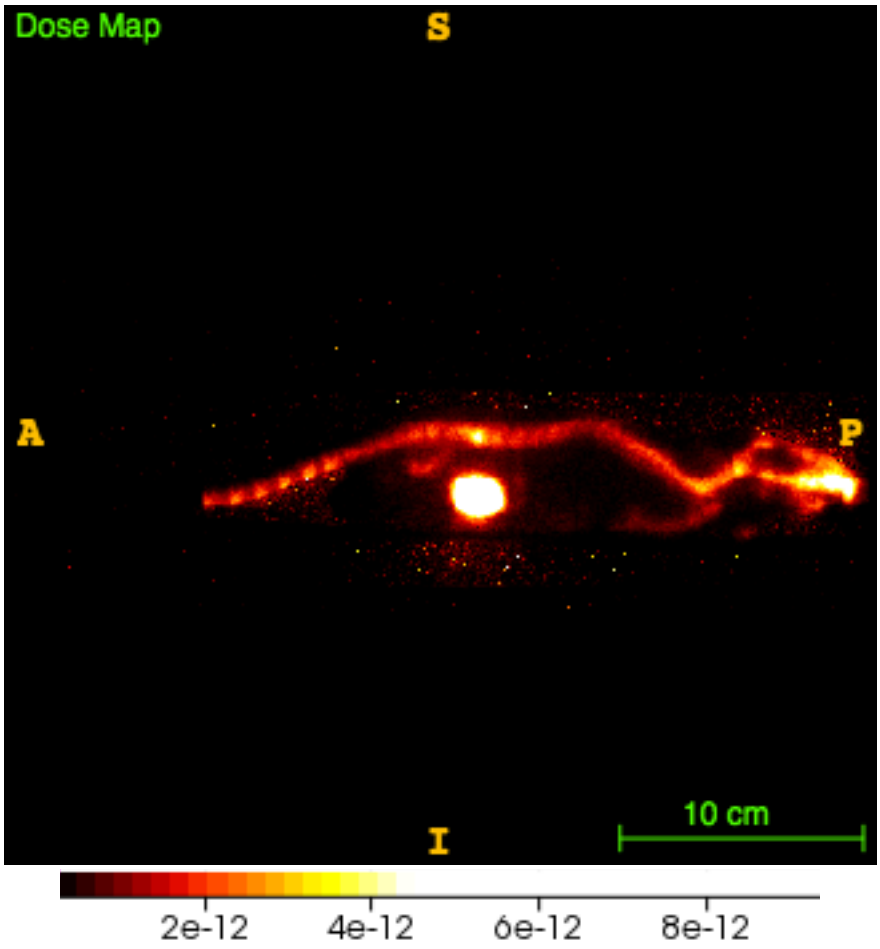

Figure 40. Slice image of the co-registered dose and micro-CT for the animal study using [^{18}F]NaF.

With a different PET tracer used, and therefore a different source starting position, a different dose map from the [^{18}F]FDG study is expected and achieved. While the range of doses to each voxel remained similar between the two studies, the locations of the highest doses are quite different. In Figure 40, there is a much higher concentration of dose around the bone regions, which is expected since that is where more particles originate. Very low regions of dose, comparable to that of air, are also

seen in the body during this study which were not seen in the last study. This is again due to the source distribution where [^{18}F]FDG will go to active metabolic sites throughout the body, while [^{18}F]NaF focuses solely on the bones.

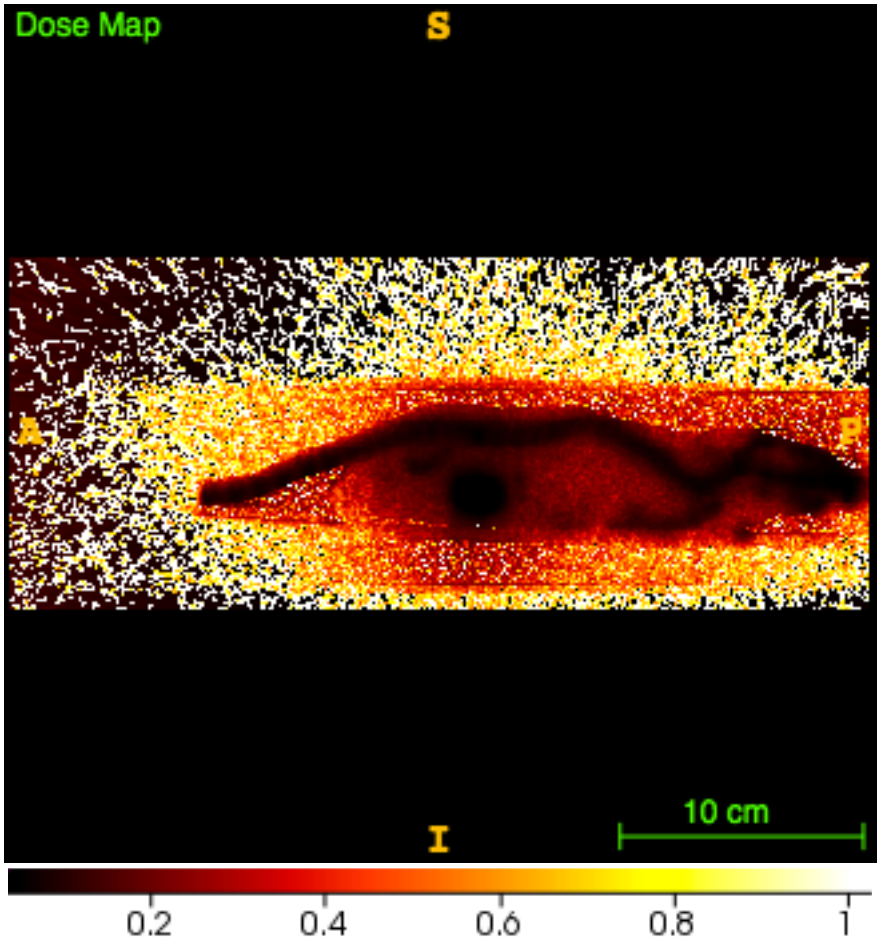

Figure 41. Slice image of the co-registered dose relative error and micro-CT for the animal study using [^{18}F]NaF.

The maximum error in the dose calculations is 1 and high errors are seen throughout the image. With the PET tracer being so localized to the bone many more

particles need to be run for this study to decrease the subject area's relative error below the required levels. The maximum relative error currently inside the subject is below 0.30. More computational time could be dedicated but was deemed unnecessary at this time.

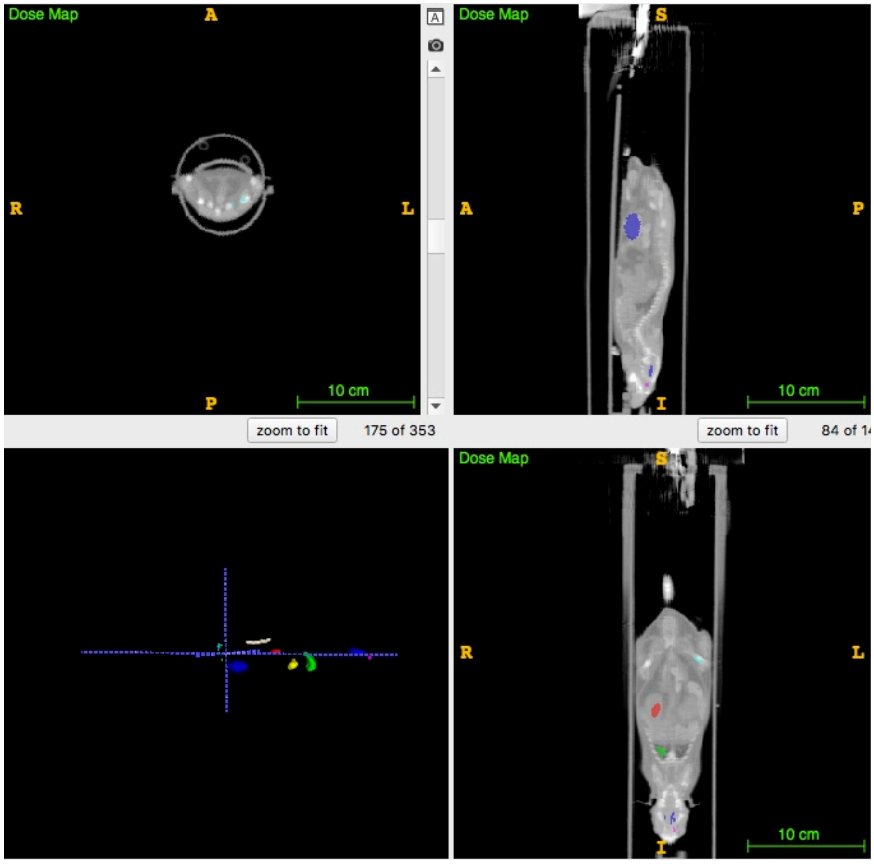

Figure 42. Segmentation performed in ITK-SNAP provided mean values for the absorbed dose in different potential organs of interest for the animal study using [18F]NaF. Kidney is marked in red, Lung in green, Brain in blue, Heart in yellow, Bone – Femur in neon blue, Eye in pink, Bone – Spine in khaki, and Bladder in dark blue.

Rough segmentation was again performed on the images to determine mean absorbed dose values to potential organs of interest. Figure 42 shows the segmentation labels on top of the micro-CT slices as well as a 3D image of the regions in the bottom right corner. Table 14 gives the mean absorbed dose values for each region along with their standard deviation.

Table 14. Absorbed dose estimates of [^{18}F]NaF for different target regions. The regions were delineated using the micro-CT images ITK-SNAP.

Tissue	Absorbed Dose (Gy Bq^{-1} s^{-1})	STD (Gy Bq^{-1} s^{-1})
Kidney	6.98×10^{-13}	3.02×10^{-13}
Lung	4.70×10^{-13}	2.62×10^{-13}
Brain	6.10×10^{-13}	2.50×10^{-13}
Heart	2.10×10^{-13}	1.23×10^{-13}
Bone - Femur	2.75×10^{-12}	1.15×10^{-12}
Eye	1.39×10^{-12}	4.78×10^{-13}
Bone - Spine	3.85×10^{-12}	6.76×10^{-13}
Bladder	3.53×10^{-11}	1.27×10^{-11}

Comparing the [^{18}F]FDG tracer absorbed dose values to the [^{18}F]NaF absorbed dose values gives the expected results. There is a higher bone – spine and bone – femur dose since this tracer attaches to these regions with a higher affinity. The dose to the bladder remains similar in both studies because anything that is not up taken in the body will go to the bladder for excretion. The dose to all other areas of interest remain lower than the values in the precious study. The heart and kidneys both receive lower absorbed doses in this study than they did in the previous study. This shows the effects of

choosing the correct radio-labeled tracer for when conducting longitudinal studies. The absorbed doses to regions of interest change depending on that choice.

4 DISCUSSION

4.1 Micro-CT

The goal of this work was to characterize a system that ideally needs to be invariant. This means it should be capable of providing, with high accuracy, the physical characteristic and resolution of the tissue types encountered in an animal model based on HU values obtained from CBCT. The present study showed that CBCT still has significant deficiencies when determining resolution, tissue composition and density of tissues. The HU values observed in CBCT were dependent on phantom geometry, generating significant variability for the same tissue type depending on phantom size and location, which presented in the form of "cupping" artifacts and large variations in HU values. Unlike clinical CT scanners, the reconstruction algorithm utilized by CBCT in the present study was not capable of correcting for beam hardening effects. The kVp values used by the Oxford Apogee x-ray unit are lower than those encountered in clinical CT x-ray units and the scanning method (axial versus conical) is quite distinct. Therefore, correction for "cupping" artifacts under CBCT remains a significant problem in image reconstruction.

Significant differences were observed between scanning phantoms (CISR versus QRM) which indicate that tissue quantitation by CBCT will require further research in addressing such differences in scanning geometry as the materials are standard for each phantom. The resulting difference in HU values for each phantom study indicates that quantitation of tissues is still a significant metrological problem due to geometry and

consequent beam hardening effects. The corresponding tissue characterization becomes very uncertain depending on what calibration setting is used in the micro-CT. The resolution of the system and corresponding noise was also a significant issue in tissue characterization. The application of smoothing filters for tissue homogenization is not recommended as it removes the tissue interface between important organs and regions of the animal model, which in turn will make it more difficult to differentiate small organs and tissues, such as the lungs, trachea and esophagus when necessary. An example of this differentiation is shown in Figure 43.

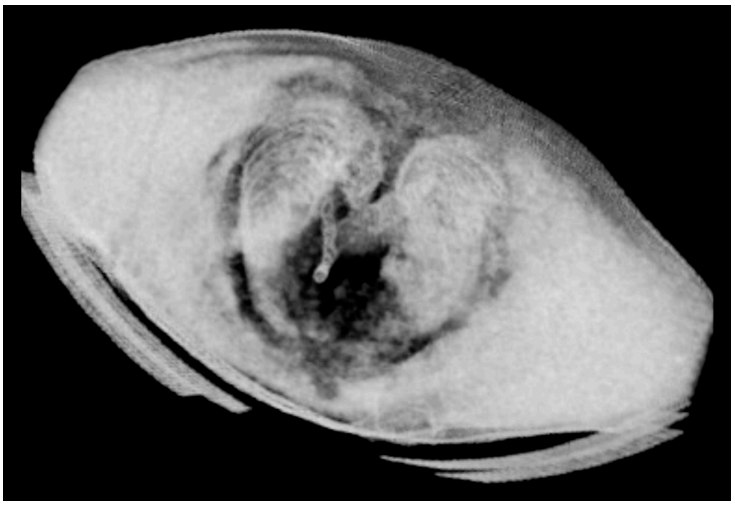

Figure 43. High resolution CBCT image for the chest of a mouse model showing a clear demarcation of the lungs, trachea and esophagus. The acquisition setting was 600 projections.

The HU values resulting from CBCT studies using different phantom indicate that significant issues remain to be addressed when using CBCT. All the issues are

associated with high density objects, specifically bone structures. The correlation of measured HU versus density is quite linear from air through the dense bone region even though expected values show that there should be at least three different linear trends. There should be a linear trend between air and water, water and dense tissue types, and dense tissue types and bone. This is due to the calibration algorithm used in the machine which forces all measured values to appear within the same linear trend line. Much higher standard deviations or noise levels are seen in materials with increasing HU value. This is driven by CBCT "cupping" effects at high HU values. Moreover, tissue differentiation between breast and adipose is not possible due to the small difference in average HU value of each material and the large uncertainty that accompanies it. Muscle and liver also have a similar issue. These uncertainties are then translated into the tissue properties and uncertainty on dosimetry calculations using Monte Carlo transport methods. In metrological terms, the use of CBCT for the characterization of tissues in animal models of diseases is a substandard metrological modality.

The superficial and deep absorbed doses at 45 kVp at low and high current were also estimated. It was found that the absorbed dose delivered per standard scan are higher by a factor of 6 and 10 for the deep and superficial dose when compared with a nominal clinical CT scan. Higher superficial doses could lead to acute and late skin tissue effects, such erythema, squamous skin discharge, and inflammatory processes. These are all confounding factors that will interfere when studying the animal models of disease.

4.2 Positron Emission Tomography

The metrology of micro-PET in animal models of diseases was studied in terms of its resolution capacity based on MLEM reconstruction iterations and activity quantitation. The resolution of the micro-PET depended on the radioisotope in question. Fluorine-18 was the focus for this specific case; however, the same methods are required to assess the resolution for other radionuclides if deemed necessary. For example, ^{124}I emits significant photons that will generate random coincidences in the PET detectors, which will decrease the resolution no matter how many iterations are used in the MLEM reconstruction algorithm. Figure 44 show a comparison of Derenzo phantom studies between ^{18}F and ^{124}I, which clearly show the loss of resolution by ^{124}I using the same number of iterations. The nominal resolution at 10% obtained for ^{18}F an ^{124}I using the Derenzo phantom was 0.75 mm and 1.25 mm, respectively. The lack of resolution is an intrinsic issue in the metrology of radionuclides in small animal models. The limiting factor continues to be the radionuclide photon spectrum quality (cleanliness), the PET detectors used, and the acceptance window of coincidence. Decreasing the acceptance window of coincidence, such as 40% to 20%, leads to a potential minimal increase in resolution and a significant increase in acquisition time, which may be detrimental to an animal under anesthesia. Therefore, the choice of radionuclide for molecular imaging needs to be carefully studied before embarking on a longitudinal study.

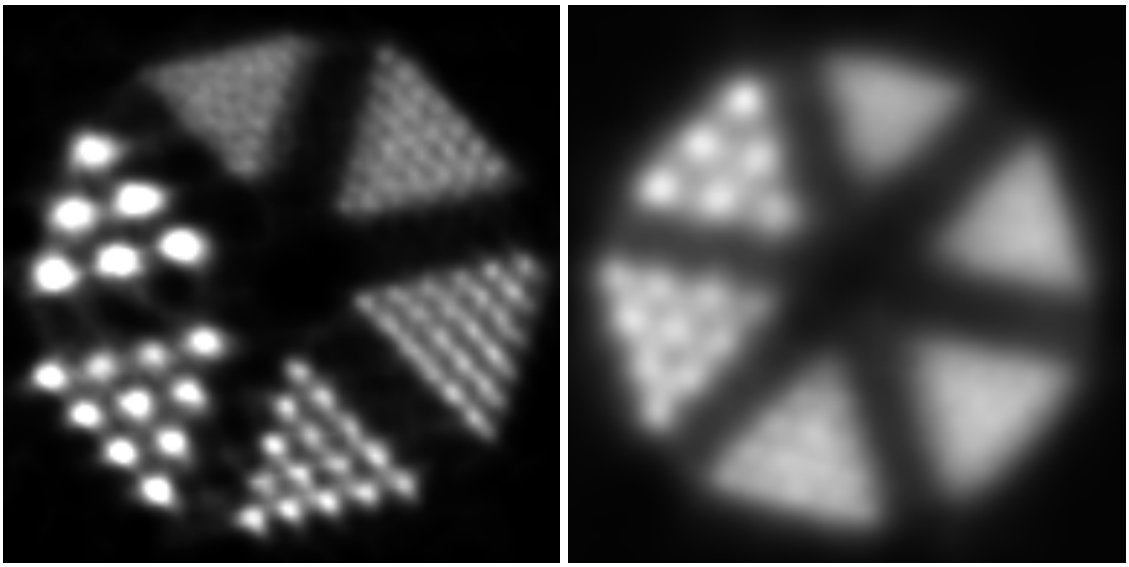

Figure 44. Derenzo phantom studies showing the difference in resolution between ^{18}F (left – 10767 kBq, MLEM 120 iterations, voxel size 0.4 mm) and ^{124}I (right – 2960 kBq, MLEM 120 iterations, voxel size 0.5 mm).

Once an image has been finalized, the next step is to convert the quantitative image given in counts per milliliter, into activity per milliliter. This process required the use of a calibration factor, Q, which was able to transform the image count data into activity data. It was observed that the calibration of the micro-PET for quantitative imaging was not simple. The plot of activity concentration versus mean counts showed an initial region of linearity, up to 80 kBq ml^{-1}, followed by a region of saturation and under-response, up to 220 kBq ml^{-1}, and ending in a region of supra-linearity above 220 kBq ml^{-1}. This study indicates that micro-PET systems are not always optimal systems. Quantification is necessary, as the data collected in the regions of saturation and supra-linearity will probably be of no significance. Therefore, administered activities to the animal models at the time of imaging shall not be higher than 7400 kBq (200 μCi).

Higher administered activities at the time of imaging will results in an unstable micro-PET system that will encounter significant dead times, an unreliable sinogram, and corresponding uncertainties or errors in reconstructed images. Therefore, the micro-PET system can only be utilized with precision and accuracy when the activity present in the system is below 7400 kBq (200 μCi).

4.3 micro-CT and micro-PET Image Registration and Uncertainty

Co-registration of images is still a significant problem in preclinical molecular imaging. Lack of co-registration alignment will yield a poor or wrong image reconstruction, as the attenuation maps used from the CT for PET reconstruction will be incorrect. This in turn may assign regions or organs with an incorrect activity that will lead to an incorrect absorbed dose calculation. The cross-capillary method was found to be a cheap and efficient to determine fine locations points in each image which could be co-registered. This test can quickly and easily be performed to assure the user that the coordinate systems of each subsystem are correctly aligning. An error in co-registration would inherently decrease the resolution of the PET images even more, shifting the measured counts further away from their true location. The higher the accuracy achieved in co-registration the higher the accuracy of the absorbed dose map generated.

4.4 Computational Assessment of Subject Absorbed Dose

The creation of a voxelized model in MCNP using a subjects CT to create the material and density maps and the PET to create the subjects source terms is fairly

simple. MCNP can now handle up to ~200+ million voxels. While the micro-PET/CT only contain ~2.8 million, clinical scans can be upwards of ~40 million. The more voxels used the more computational time required to achieve values with acceptable relative errors. Runs in the current study take two to five days depending on the number of computer cores available for processing. If energy deposition in each voxel was not required, but rather the deposition in certain materials, or organs, the computer time would be decreased but information about specific voxels would be lost.

With the calibration of the micro-CT machine the HU range was used to convert into material composition and density for use in MCNP. This requires translating a range of over 2000 HU values into 24 different material bins. With finer differences in tissue HU values and less system noise the material information used could be more defined leading to more accurate results. Creating finer bins with more density and composition accuracy would require a more in-depth study into the x-ray spectrum of the machine and its calibration factors for calculating HU values based off of the spectrums measured during the scans.

Segmentation was shown to be possible with the absorbed dose maps generated from the MCNP values. The whole subject or specific regions can be chosen to calculate specific absorbed doses. The only information required by the user is the injected activity in Bq and the amount of time doses should be calculated over in seconds. For example, the whole body mean absorbed dose for the study using [^{18}F]FDG with an injected activity of 7400 kBq and an imaging time of one hour was 4.2 cGy. Incorporating the absorbed dose from the CT scan the total absorbed dose to the patient

during the imaging study can be monitored. The ability to obtain these specific values could lead to more accurate studies and easier translation to the clinical level.

4.5 Applications in Animal Models of Diseases

Depending on the type of disease and the treatment model different organs become the limiting factor. These limiting regions include the brain, heart, and bone marrow. The absorbed doses to these regions dictate the treatment doses that can be delivered to the target area. Absorbed doses to these organs and tissues must be tracked and accounted for when implementing longitudinal imaging studies focused on these areas so as to better distinguish effects from treatment versus effects from imaging.

4.5.1 Radiation-Induced Cardiac Toxicity

Radiation induced cardiac toxicity (RICT) or radiation-induced heart disease (RIHD) is a significant burden on patients that have undergone radiotherapy of the chest or other close by organs, such as those patients with breast cancer and Hodgkin's lymphoma. RIHD includes a wide spectrum of pathologies, such as coronary artery disease, myocardial dysfunction, valvular disorders, and pericardial disease. The prevalence of RIHD varies among studies with between 20 – 40 % of patients mostly suffering from pericardial effusion [70, 71]. Damage to the myocardium is primarily caused by damage to the microvasculature due to capillary loss. The risk of developing RIHD is higher in young patients (< 20 y). Experimental animal studies have shown that radiation doses of > 2 Gy are associated with increased expression of various

inflammatory cytokines and adhesion molecules in endothelial cells of both the microvasculature and large vessels [72]. However, under the paradigm of hormesis, it has been shown that whole-body doses of 0.1–0.6 Gy have been shown to inhibit leukocyte adhesion to endothelial cells in rats, and doses of 0.025–0.05 Gy exerted some protective effects on the development of atherosclerosis in ApoE-/- mice, particularly at low dose rates [72]. Animal models are being used to develop radio-protectants strategies against RIHD, which are capable of minimizing the acute and long term effects [73].

In this study the total absorbed doses to the heart from combined micro-CT and micro-PET exposures were estimated at 0.3 Gy for a single imaging session using [^{18}F]FDG. Over multiple imaging time points this could become a significant cumulative absorbed dose that becomes a confounding factor in cardiac toxicity studies. It would even be possible to go back to previous studies to determine specific organ absorbed dose values at a later date when symptoms or effects begin to present as long as images are stored with acquisition information (injected activity, scan time, etc.). The threshold for inducing cardiac toxicity depending on time of induction can be between 2 to 20 Gy [71].

4.5.2 Radiation-Induced Brain Toxicity

During the treatment of head and neck tumors the limiting organ is the brain. In imaging, [^{18}F]FDG goes to areas of high metabolic activity which includes the brain. For repeated longitudinal studies the absorbed doses to this region can become significant.

As seen from calculations, the dose to the brain during a single PET scan using [^{18}F]FDG results in an absorbed dose of around 0.1 Gy. Monitoring of the absorbed dose value can lead to more accurate conclusion being drawn about the effects of the study target.

4.5.3 Hematopoietic Toxicity

Within the bone marrow the effects of absorbed dose are relative to the amount of absorbed dose where even small doses can lead to measureable reductions in the proliferative capacity of bone marrow stem cells. Early studies in dogs have shown that a dose rate of 0.075 Gy/day represents a threshold below which the blood-forming system retains its capacity for cell production for at least 1 year; however, at doses of > 0.075 Gy/day, nearly 60% of the irradiated dogs died from progressive aplastic anemia in less than 300 days. In rats and mice exposed to long-term irradiation at doses of 0.01–0.5 Gy/day (cumulative doses of 2–30 Gy) showed that the earliest and greatest depopulation occurred in the multipotent stem cell compartment [spleen colony-forming units (CFU-S)], which led to depletion of committed precursor cells and then of the functional cell pool. Long-term exposure induces depletion of the bone marrow stem cell compartment and increases proliferative activity of these cells. Experiments in rodents show that increased proliferative activity of multipotent CFU-S occurs after exposure doses of 0.2–0.3 Gy; this leads to increased numbers of committed precursor cells and differentiated cells. Chronic exposures also stimulate proliferative activity in the committed precursor cells. Therefore, when molecular imaging studies are carried

out, consideration of doses to the bone marrow and spleen need to be well determine in order to assess any confounding factors that may be added to the research paradigm. The experimental evidence indicates that an acute threshold dose of 0.5 Gy be used for hematopoietic toxicity. The spleen and bone marrow can be carefully segmented out of a CT image and should appear as regions of higher activity using [^{18}F]FDG in a PET scan. Unfortunately, the size of the structures makes monitoring these dose levels difficult without finer resolution in the imaging modalities. In our present [^{18}F]FDG study the absorbed dose to the spine was estimated at 4.4 cGy and 3 cGy to the femur. If multiple studies are carried out, then the total cumulative dose to the bone marrow will be significant and comparable to the doses where hematological toxicity may be of concern.

4.5.4 Animal Models of Regenerative Medicine

Cell-based regenerative medicine therapies (RMTs) and their translation to clinical application are a major focus of research and play a key role in future clinical practice. Cell-based RMTs include various cell types, such as stem cells, stromal cells, and macrophages and have the potential to treat multiple diseases. Many RMTs have shown great promise in preclinical studies for various diseases, including kidney and liver diseases and myocardial infarction; however, translation into the clinic has been limited. The slow translation from bench-to-bedside is due to the lack of convincing animal models and reproducible data on the safety, efficacy and mode of action of RMTs.

Relevant rodent animal models are needed to gain an understanding of both the efficacy and the safety of cell-based RMTs. Current methods generally rely on *ex vivo* histological analysis of tissues post-mortem. This approach requires many animals to be sacrificed at multiple time points in order to gain a comprehensive insight into *in vivo* processes. Importantly, it does not allow researchers to monitor individual animals over the course of their treatment. This need is being addressed by using molecular imaging methods that monitor the longitudinally response of every animal thus minimizing animal use and acquiring higher fidelity morphological and physiological data.

There are multiple animal models of regenerative medicine depending on the target organ to be considered. The use of micro-PET/CT provides high sensitivity morphological and physiological data, which is an advantage for tracking anatomical localization of stem cells and PET imaging and using reporter genes permits long-term studies. By directly labeling cells with PET probes, such as ^{18}F, ^{64}Cu, or ^{124}I it is possible to monitor the fate of these labeled cells throughout the body, including their proliferation. Because of the high sensitivity of the micro-PET/CT, it is possible to detect as few as 10 labeled cells with a minimum activity 0.1 kBq. However, the absorbed doses delivered by the micro-CT are of great significance and may induce changes in multiple organs and tissues by inducing radiobiological changes in the microenvironment and stem cells. Stem cells have been labeled with PET probes to assess their fate in the hippocampus for brain function, in the kidneys, lungs and bone marrow [74].

4.6 Advantages and Limitations of micro-CT versus micro-MRI

Most of the issues and disadvantages discussed with micro-CT above can be resolved by the use of a micro-MRI. The move from micro-CT to micro-MRI imaging is currently being commercialized by one commercial company, Bruker Biospin, Inc. In pre-clinical imaging studies, scanning times required for MRI imaging are similar to those of micro-PET, which are around 60 min; thus, the simultaneous acquisition of the PET and MRI will be similar. A list of the advantages of both modality types is given in Table 15. The benefits of MRI are higher tissue characterization and differentiation, inclusion of functional imaging and spectroscopy, use of radioactive and non-radioactive binary probes, and no radiation exposure from x-rays. Clearly, the ability to discriminate between tissues greatly increase the accuracy of calculated absorbed doses. However, the long scan times produce some blurring on active organs and tissues regions of the body, such as the lungs and heart. The MRI signal will be the average value at the target location over the scanning time instead of the more accurate representation of the faster CT imaging modality, which would incorporate less motion. As an example, Figure 45 shows the acquired micro-PET/MRI image for comparison to the micro-PET/CT images displayed in the present work. MRI images provide a significant advantage for tissue segmentation when compared to CT images.

Table 15. Advantages of hybrid PET/MRI versus PET/CT in small animal imaging.

Attribute	Micro-PET/MRI advantages	Micro-PET/CT advantages
Lesion detection	Improved lesion detection (i.e. colorectal, lung, osteosarcoma, and bony metastases)	No advantage
Lesion margins	Better delineation of tumors and classification	Improved delineation of lesion margins within lung parenchyma
Lesion alignment	Better alignment of simultaneously acquired PET/MRI data when compared with PET/CT	No advantage
Quantitative analysis	Improved quantification by MRI-based motion correction without additional radiation	Current standard based on density seen on CT
Scanning time	No advantage	Micro-PET/CT scanning protocols are currently faster
Radiation exposure	No CT reduces radiation exposure to animals	No advantage
Animal accessibility	Simultaneous acquisition (PET insert)	In line
Multi-parametric analysis	Expanded capabilities such as DWI, perfusion MRI, fMRI, MR spectroscopy, and use of binary or multiple MRI and PET probes	No advantage

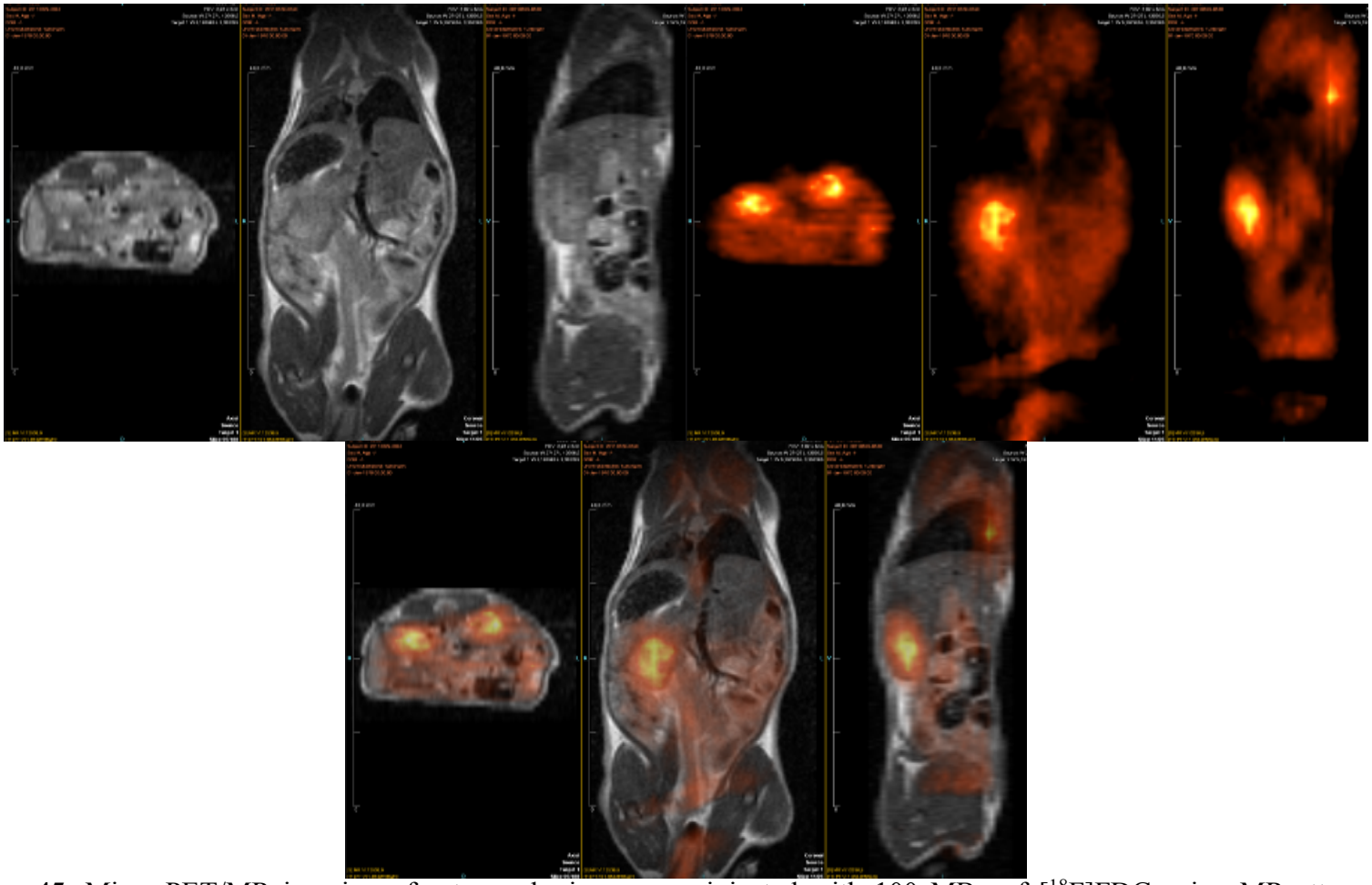

Figure 45. Micro-PET/MR imaging of a tumor-baring mouse injected with 100 MBq of [^{18}F]FDG using MR attenuation correction mapping. Acquisition time of 600 sec.

5 CONCLUSIONS

5.1 General Conclusions

In this work, we have established the necessary tools for creating a quantitated system encompassing not only the imaging units of the micro-PET/CT but also the quantitation of activity distribution and dosimetry of the imaged animal as well. To begin the subsystems were quantified for their response to changes in the imaging object. For the micro-CT this included understanding the relationship between tissue type, composition, and density and how it related to the values provided in the CT images after reconstruction. The absorbed doses for different micro-CT scanning methods were also measured so as to gain the ability to track subject dose reviewed from the whole imaging study, CT and PET combined.

The micro-PET system was quantified next to gain an understanding of the resolution of the subsystem and explore the capabilities and limitations of the machine when applying radiolabeled tracers. Once this characterization was determined, the system was evaluated for its count response versus activity over time. It was observed that the micro-PET system does not respond linearly as function of activity concentration. Regions of linearity, supra-linearity, and saturation were all observed. The response allowed for the counts in a reconstructed PET image to be converted to an activity concentration, but only as long as the concentration remained in the linear region of the plot. This region of linearity limited the total injected activity at the time of imaging to be no more than 7400 kBq (200 μCi).

With each subsystem characterized separately, the image co-registration of the modalities was then measured to verify that the coordinate systems of each system were correctly aligned within 1 mm. A cross-capillary method was used to determine the offset in the *x*, *y*, and *z* directions which were later used as correction factors when aligning the images during co-registration. This ensures a correct PET reconstruction with the correct attenuation map, as well as the attribution of the correct amount of activity concentration to the true voxel location in the CT image.

Once the whole systems response to imaged subject was quantified the data was used to generate an input deck for MCNP6 to calculate the dose received by each voxel from the radiolabeled tracer injected during the imaging study. Two different tracers were studied, and the results showed the expected differences between the two. The [^{18}F]FDG study, and delivered high absorbed doses to the kidney's, heart, and brain. On the other hand, the [^{18}F]NaF study delivered high absorbed doses to bone surfaces. With the generation of animal specific absorbed dose maps, investigators can segment tissues or a region of interest for further dosimetry analysis. This can allow the dose to a particular organ or tissue to be tracked across an entire longitudinal study of the animal and be included in the analysis on the effectiveness of treatment options tested. In the present study, the radionuclide selected was ^{18}F; however, it is possible to carry out the same procedures for other radionuclides, such as ^{124}I as long as the source distribution tracer is deemed to be the same distribution the radionuclide of interested in known to have.

5.2 Future Work

The first step in continuing this work is to more fully understand the micro-CT detector response to materials. If the material information can be known with greater accuracy the creation of materials in MCNP becomes more accurate as well as the results it produces. The implementation of this process on a different pre-clinical machine and the ability to measure the same subject and compare results would further corroborate the claims made in this research. Finally, the implementation of this work in longitudinal studies to determine if dose thresholds for specific radiation effects are reached would show the necessity for the ability to track organ specific absorbed dose values across multiple time points in a longitudinal study.

REFERENCES

1. Sunderland, J.J. and P.E. Christian, *Quantitative PET/CT scanner performance characterization based upon the society of nuclear medicine and molecular imaging clinical trials network oncology clinical simulator phantom.* Journal of nuclear medicine : official publication, Society of Nuclear Medicine, 2015. **56**(1): p. 145-152.

2. Nordstrom, R.J., *Special Section Guest Editorial: Quantitative Imaging and the Pioneering Efforts of Laurence P. Clarke.* Journal of Medical Imaging, 2017. **5**(1): p. 011001.

3. Nordstrom, R.J., *The Quantitative Imaging Network in Precision Medicine.* Tomography : a journal for imaging research, 2016. **2**(4): p. 239-241.

4. Kalpathy-Cramer, J., et al., *Quantitative Imaging Network: Data Sharing and Competitive AlgorithmValidation Leveraging The Cancer Imaging Archive.* Translational oncology, 2014. **7**(1): p. 147-152.

5. Farahani, K., et al., *Computational Challenges and Collaborative Projects in the NCI Quantitative Imaging Network.* Tomography : a journal for imaging research, 2016. **2**(4): p. 242-249.

6. Clarke, L.P., et al., *The Quantitative Imaging Network: NCI's Historical Perspective and Planned Goals.* 2014. **7**(1): p. 1-4.

7. D'Arienzo, M. and M. Cox, *Uncertainty Analysis in the Calibration of an Emission Tomography System for Quantitative Imaging.* Computational and mathematical methods in medicine, 2017. **2017**: p. 9830386.

8. Billas, I., et al., *Development of a primary standard for absorbed dose from unsealed radionuclide solutions.* 2016. **53**(6): p. 1259.

9. Jha, A.K., et al., *Practical no-gold-standard evaluation framework for quantitative imaging methods: application to lesion segmentation in positron emission tomography.* Journal of Medical Imaging, 2017. **4**(1): p. 011011.

10. Scheuermann, J.S., et al., *Qualification of National Cancer Institute-Designated Cancer Centers for Quantitative PET/CT Imaging in Clinical Trials.* Journal of nuclear medicine : official publication, Society of Nuclear Medicine, 2017. **58**(7): p. 1065-1071.

11. Kurland, B.F., et al., *Multicenter Clinical Trials Using 18F-FDG PET to Measure Early Response to Oncologic Therapy: Effects of Injection-to-Acquisition Time Variability on Required Sample Size.* J Nucl Med, 2016. **57**(2): p. 226-30.

12. Adiseshaiah, P., et al., *A novel gadolinium-based trimetasphere metallofullerene for application as a magnetic resonance imaging contrast agent.* Invest Radiol, 2013. **48**(11): p. 745-54.

13. Chapman, S., et al., *Nanoparticles for cancer imaging: The good, the bad, and the promise.* Nano Today, 2013. **8**(5): p. 454-460.

14. Crist, R.M., et al., *Common pitfalls in nanotechnology: lessons learned from NCI's Nanotechnology Characterization Laboratory.* Integr Biol (Camb), 2013. **5**(1): p. 66-73.

15. Dobrovolskaia, M.A. and S.E. McNeil, *Understanding the correlation between in vitro and in vivo immunotoxicity tests for nanomedicines.* J Control Release, 2013. **172**(2): p. 456-66.

16. Dobrovolskaia, M.A., et al., *Choice of method for endotoxin detection depends on nanoformulation.* Nanomedicine (Lond), 2014. **9**(12): p. 1847-56.

17. Ilinskaya, A.N. and M.A. Dobrovolskaia, *Nanoparticles and the blood coagulation system. Part II: safety concerns.* Nanomedicine (Lond), 2013. **8**(6): p. 969-81.

18. Ilinskaya, A.N. and M.A. Dobrovolskaia, *Nanoparticles and the blood coagulation system. Part I: benefits of nanotechnology.* Nanomedicine (Lond), 2013. **8**(5): p. 773-84.

19. Janib, S.M., A.S. Moses, and J.A. MacKay, *Imaging and drug delivery using theranostic nanoparticles.* Adv Drug Deliv Rev, 2010. **62**(11): p. 1052-1063.

20. Dobrovolskaia, M.A. and S.E. McNeil, *Strategy for selecting nanotechnology carriers to overcome immunological and hematological toxicities challenging clinical translation of nucleic acid-based therapeutics.* Expert Opin Drug Deliv, 2015. **12**(7): p. 1163-75.

21. Akhtar, A., *The flaws and human harms of animal experimentation.* Camb Q Healthc Ethics, 2015. **24**(4): p. 407-19.

22. Schatten, H. and G.M. Constantinescu, *Animal models and human reproduction*. 2017, Hoboken, New Jersey: Wiley/Blackwell. xviii, 578 pages, 12 unnumbered pages of plates.

23. Chan, C.-C., *Animal models of ophthalmic diseases*. Essentials in ophthalmology,. 2016, Cham: Springer. xv, 152 pages.

24. Martínez-Murillo, R. and A. Martínez, *Animal models of brain tumors*. Neuromethods,. 2013, New York: Humana Press ; Springer. xiii, 391 p.

25. Avena, N.M., *Animal models of eating disorders*. Neuromethods,. 2013, Totowa N.J.: Humana Press. xvi, 379 p.

26. Aldskogius, H.k., *Animal models of spinal cord repair*. Neuromethods. 2013, New York: Humana Press ; Springer. xii, 366 p.

27. Chen, J., *Animal models of acute neurological injuries : injury and mechanistic assessments*. Springer protocols. 2012, New York: Humana Press.

28. Olmstead, M.C., *Animal models of drug addiction*. Neuromethods,. 2011, New York: Humana Press. xii, 484 p.

29. O'Donnell, P., *Animal models of schizophrenia and related disorders*. Neuromethods,. 2011, New York: Humana Press. xii, 290 p.

30. New York Academy of Sciences., *Animal models : their value in predicting drug efficacy and toxicity*. Annals of the New York Academy of Sciences,. 2011, Boston, Mass.: Published by Blackwell Pub. on behalf of the New York Academy of Sciences. 64 p.

31. Ma, C. and J.-M. Zhang, *Animal models of pain*. Neuromethods,. 2011, New York: Humana Press. xii, 204 p.

32. Lane, E.L. and S.B. Dunnett, *Animal models of movement disorders. Volume I*. Neuromethods,. 2011, Totowa, N.J.: Humana Press. xv, 447 p.

33. Lane, E.L. and S.B. Dunnett, *Animal models of movement disorders. Volume II*. Neuromethods,. 2011, New York: Humana Press. xv, 443 p.

34. Deyn, P.P.d. and D.v. Dam, *Animal models of dementia*. Springer protocols. 2011, New York: Humana Press. xv, 732 p.

35. Avila, J.s., et al., *Animal models for neurodegenerative disease*. RSC drug discovery series,. 2011, Cambridge: Royal Society Chemistry. xv, 290 p.

36. Pang, I.-H. and A.F. Clark, *Animal models for retinal diseases*. Neuromethods,. 2010, Totowa, N.J.: Humana Press. xii, 229 p.

37. Chen, J., *Animal models of acute neurological injuries*. 2009, Totowa, NJ: Humana Press. xxi, 498 p.

38. Bizon, J.L. and A.G. Woods, *Animal models of human cognitive aging*. 2009, New York: Humana Press. xii, 208 p., 4 p. of plates.

39. Baraban, S.C., *Animal models of epilepsy : methods and innovations*. Neuromethods,. 2009, New York: Humana Press. xiii, 272 p.

40. Shafrir, E., *Animal models of diabetes : frontiers in research*. 2nd ed. 2007, Boca Raton: CRC Press. 365 p.

41. Gold, A. and Y. Dudai, *Simulation of Mental Disorders: I. Concepts, Challenges and Animal Models.* Isr J Psychiatry Relat Sci, 2016. **53**(2): p. 64-71.

42. Le Magnen, C., A. Dutta, and C. Abate-Shen, *Optimizing mouse models for precision cancer prevention.* Nat Rev Cancer, 2016. **16**(3): p. 187-96.

43. Fox, J.G., *The mouse in biomedical research*. 2nd ed. 2007, Amsterdam ; Boston: Elsevier.

44. Kato, T. and S. Takada, *In vivo and in vitro disease modeling with CRISPR/Cas9.* Brief Funct Genomics, 2017. **16**(1): p. 13-24.

45. Dow, L.E., *Modeling Disease In Vivo With CRISPR/Cas9.* Trends Mol Med, 2015. **21**(10): p. 609-21.

46. Mou, H., et al., *Precision cancer mouse models through genome editing with CRISPR-Cas9.* Genome Med, 2015. **7**(1): p. 53.

47. Simon, R., *Sensitivity, Specificity, PPV, and NPV for Predictive Biomarkers.* J Natl Cancer Inst, 2015. **107**(8).

48. Biomarkers Definitions Working, G., *Biomarkers and surrogate endpoints: preferred definitions and conceptual framework.* Clin Pharmacol Ther, 2001. **69**(3): p. 89-95.

49. European Society of, R., *White paper on imaging biomarkers.* Insights Imaging, 2010. **1**(2): p. 42-45.

50. Sullivan, D.C., et al., *Metrology Standards for Quantitative Imaging Biomarkers.* Radiology, 2015. **277**(3): p. 813-25.

51. *Quantitative Imaging Biomarkers Alliance.* 2017; Available from: https://www.rsna.org/QIBA/.

52. European Society of, R., *ESR statement on the stepwise development of imaging biomarkers.* Insights Imaging, 2013. **4**(2): p. 147-52.

53. O'Connor, J.P., et al., *Imaging biomarker roadmap for cancer studies.* Nat Rev Clin Oncol, 2017. **14**(3): p. 169-186.

54. Feldkamp, L.A., L.C. Davis, and J.W. Kress, *Practical cone-beam algorithm.* Journal of the Optical Society of America A, 1984. **1**(6): p. 612-619.

55. BioSpin, B., *Albira Si*, B. BioSpin, Editor. 2016.

56. Perry, B.J. and C. Bridges, *Computerized transverse axial scanning (tomography). 3. Radiation dose considerations.* Br J Radiol, 1973. **46**(552): p. 1048-51.

57. Ambrose, J., *Computerized transverse axial scanning (tomography). 2. Clinical application.* Br J Radiol, 1973. **46**(552): p. 1023-47.

58. Hounsfield, G.N., *Computerized transverse axial scanning (tomography): Part I. Description of system. 1973.* Br J Radiol, 1995. **68**(815): p. H166-72.

59. Medicine, Q.A.i.R.a. *Micro-CT HA Phantom*. 2008; Available from: http://www.qrm.de/content/products/microct/microct_ha.htm.

60. Swennen, G.R. and F. Schutyser, *Three-dimensional cephalometry: spiral multi-slice vs cone-beam computed tomography.* Am J Orthod Dentofacial Orthop, 2006. **130**(3): p. 410-6.

61. Pemler, P., U. Schneider, and J. Besserer, *[Evaluation of the electron density phantom CIRS Model 62].* Z Med Phys, 2001. **11**(1): p. 25-32.

62. International Commission on Radiation Units and Measurements., *Tissue substitutes in radiation dosimetry and measurement*. ICRU report. 1989, Bethesda, Md., U.S.A.: International Commission on Radiation Units and Measurements. vii, 189 p.

63. Poludniowski, G., et al., *SpekCalc: a program to calculate photon spectra from tungsten anode x-ray tubes.* Phys Med Biol, 2009. **54**(19): p. N433-8.

64. Poludniowski, G.G., *Calculation of x-ray spectra emerging from an x-ray tube. Part II. X-ray production and filtration in x-ray targets.* Med Phys, 2007. **34**(6): p. 2175-86.

65. Poludniowski, G.G. and P.M. Evans, *Calculation of x-ray spectra emerging from an x-ray tube. Part I. electron penetration characteristics in x-ray targets.* Med Phys, 2007. **34**(6): p. 2164-74.

66. Hubbell, J.H., S.M. Seltzer, and National Institute of Standards and Technology (U.S.). *Tables of X-ray mass attenuation coefficients and mass energy-absorption coefficients 1 keV to 20 MeV for elements Z=1 to 92 and 48 additional substances of dosimetric interest*. Nistir 5632; Web:[Available from: http://physics.nist.gov/PhysRefData/XrayMassCoef/cover.html.

67. Ma, C.M., et al., *AAPM protocol for 40-300 kV x-ray beam dosimetry in radiotherapy and radiobiology.* Med Phys, 2001. **28**(6): p. 868-93.

68. T. Goorley, M.J., T. Booth, F. Brown, J. Bull, L. J. Cox, J. Durkee, J. Elson, M. Fensin, R. A. Forster, J. Hendricks, H. G. Hughes, R. Johns, B. Kiedrowski, R. Martz, S. Mashnik, G. McKinney, D. Pelowitz, R. Prael, J. Sweezy, L. Waters, T. Wilcox, T. Zukaitis, *Initial MCNP6 Release Overview.* Nuclear Technology, 2012. **180**(3): p. 298-315.

69. Schneider, W., T. Bortfeld, and W. Schlegel, *Correlation between CT numbers and tissue parameters needed for Monte Carlo simulations of clinical dose distributions.* Phys Med Biol, 2000. **45**(2): p. 459-78.

70. Taunk, N.K., et al., *Radiation-induced heart disease: pathologic abnormalities and putative mechanisms.* Frontiers in Oncology, 2015. **5**(1): p. 39.

71. Madan, R., et al., *Radiation induced heart disease: Pathogenesis, management and review literature.* Journal of the Egyptian National Cancer Institute, 2015. **27**(4): p. 187-193.

72. Authors on behalf of, I., et al., *ICRP publication 118: ICRP statement on tissue reactions and early and late effects of radiation in normal tissues and organs--threshold doses for tissue reactions in a radiation protection context.* Ann ICRP, 2012. **41**(1-2): p. 1-322.

73. Hall, S., et al., *Protection against Radiotherapy-Induced Toxicity.* Antioxidants (Basel, Switzerland), 2016. **5**(3).

74. Scarfe, L., et al., *Preclinical imaging methods for assessing the safety and efficacy of regenerative medicine therapies.* NPJ Regen Med, 2017. **2**: p. 28.